Phase-dependent polymerization isomerism in the coordination complexes of a flexible bis(β-diketonato) ligand

Manuel Imperato,[a,b,#] Alessio Nicolini,[a,#] Matteo Boniburini,[a] Silvia Gómez-Coca,[c] Eliseo Ruiz,[c] Fabio Santanni,[d] Lorenzo Sorace,[d] and Andrea Cornia[a,*]

[a]Dipartimento di Scienze Chimiche e Geologiche e UdR INSTM, Università degli Studi di Modena e Reggio Emilia, via G. Campi 103, 41125 Modena, Italy. E-mail: acornia@unimore.it

[b]Dipartimento di Scienze Fisiche, Informatiche e Matematiche, Università degli Studi di Modena e Reggio Emilia, via G. Campi 213/A, 41125 Modena, Italy

[c]Departament de Química Inorgànica i Orgànica, Institut de Química Teòrica i Computacional Universitat de Barcelona, Diagonal 645, 08028 Barcelona, Spain

[d]Dipartimento di Chimica "Ugo Schiff" e UdR INSTM, Università degli Studi di Firenze, via della Lastruccia 3, 50019 Sesto Fiorentino (FI), Italy

Abstract. First prepared in the late 70s, the pro-ligand 1,3-bis(3,5-dioxo-1-hexyl)benzene (H_2bdhb) contains two acetoacetyl terminations linked to a central 1,3-phenylene unit through dimethylene bridges. Since each termination can be either in diketonic or keto-enolic form, in organic solution it exists as a mixture of three spectroscopically resolvable tautomers. In the presence of pyridine, Co^{2+} and the $bdhb^{2-}$ dianion form a crystalline dimeric compound with formula $[Co_2(bdhb)_2(py)_4]$ (**2**) and a Co···Co separation of >11 Å. Complex **2** contains two pseudo-octahedrally coordinated and non-interacting high-spin cobalt(II) ions ($S = 3/2$) displaying a large easy-plane anisotropy ($D \sim 70$ cm^{-1}), as consistently indicated by magnetic measurements, X-band EPR spectra, and complete active space self-consistent field/*N*-electron valence state perturbation theory (CASSCF/NEVPT2) calculations. At cryogenic temperatures ($T < 7$ K) and in an applied static magnetic field, the compound shows detectably slow magnetic relaxation, which occurs through direct and Raman mechanisms. Combined mass spectrometry, UV-Vis, and ^{1}H/^{2}H NMR data, including an isotopic labelling experiment and a determination of molecular weight by diffusion ordered spectroscopy (DOSY), show that **2** rearranges to monomeric high-spin $[Co(bdhb)(py)_x]$ species ($x = 0$, 1, or 2) in organic solution (CH_2Cl_2, THF) with concomitant partial dissociation of the py ligands. The X-band EPR spectra in a frozen CH_2Cl_2/toluene matrix concurrently suggest a significant alteration of the coordination environment upon dissolution. These observations are fairly well reproduced by density functional theory (DFT) and CASSCF/NEVPT2 calculations on the lowest Gibbs free energy conformers of each species, as

provided by an extensive conformational search based on meta-dynamics simulations and semiempirical tight-binding methods. After the vanadyl analogue, compound **2** provides the second example of polymerization isomerism in the 1:1 adducts of $bdhb^{2-}$ with divalent metal ions.

[#]These authors contributed equally to the work.

†Electronic Supplementary Information (ESI) available: details on the assignment of ^{1}H and ^{13}C NMR signals of H_2bdhb (Supplementary Note 1), additional NMR spectra (Fig. S1-S10 and Fig. S37), crystallographic data and figures (Fig. S11-S13, Tables S1 and S2), FT-IR and UV-Vis-NIR spectra (Fig. S14-S16 and S29-S33), Zeeman diagrams (Fig. S17), AC magnetic susceptibility data (Fig. S18-S24, Tables S3-S5) and details on their fitting procedure (Supplementary Note 2), additional results of DFT and CASSCF/NEVPT2 calculations (Fig. S26-S28, and S41, Tables S7 and S8), ESI-MS spectra (Fig. S34-S36), details of DOSY experiments (Fig. S38 and S39), additional EPR spectra (Fig. S25 and S40) and details on their fitting procedure (Supplementary Note 3 and Table S6), and final cartesian atomic coordinates and thermochemical data for the DFT optimized structures in Table S8. CCDC 2379443 (**2**). For ESI and crystallographic data in CIF or other electronic format see DOI: XXXXXX.

1. INTRODUCTION

In their classical textbook,[1] Greenwood and Earnshaw use the term *polymerization isomerism* to describe the relationship between two compounds having the same elemental composition but different molecular weights. Although strictly speaking not compliant with the IUPAC definition of isomerism,[2] the term is still used in coordination and organometallic chemistry.[3,4]

We have encountered unexpected examples of polymerization isomerism while working with the proligand 1,3-bis(3,5-dioxo-1-hexyl)benzene (H_2bdhb), which contains two acetoacetyl residues linked to a 1,3-phenylene unit through dimethylene bridges (Scheme 1). Its doubly deprotonated form $bdhb^{2-}$ interacts strongly with d- and f-block metals, as demonstrated in previous synthetic and solution studies;[5–8] however, to the best of our knowledge only one metal adduct of $bdhb^{2-}$ has been so far authenticated by X-ray crystallography, namely the VO^{2+} complex very recently isolated and characterized as a molecular spin qubit by some of us.[9] This compound exhibits a phase-dependent structure, as it crystallizes as dimeric [$(VO)_2(bdhb)_2$] but exists in monomeric [VO(bdhb)] form in solution. The reason is that the flexible organic backbone allows the two β-diketonato functions to bind either to the same metal ion, yielding a quasi-macrocyclic structure, or to two different metal ions, affording a dimeric structure with the two metal centers at more than 1 nm from each other.

We herein provide a detailed account of the synthesis and solution behavior of H_2bdhb, which displays multiple tautomeric forms in solutions. We then report the synthesis of two cobalt(II) complexes of $bdhb^{2-}$, namely "Co(bdhb)$(H_2O)_2$" (**1**), for which we propose a tentative structure, and [$Co_2(bdhb)_2(py)_4$] (**2**), which was isolated in crystalline form. In **2**, the two hexacoordinated and well-separated high-spin cobalt(II) ions (Co···Co >11 Å) have a large easy-plane magnetic anisotropy and display detectably slow magnetic relaxation (SMR) under an applied static magnetic field. However, this dimeric complex rearranges to monomeric high-spin [Co(bdhb)$(py)_x$] species (x = 0, 1, or 2) in organic solution (Scheme 1), as shown by a portfolio of experimental methods including electrospray ionization-mass spectrometry (ESI-MS), diffusion ordered spectroscopy (DOSY), and X-band EPR. These observations were fairly well accounted for by an extensive theoretical treatment based on density functional theory (DFT) and complete active space self-consistent field/*N*-electron valence state perturbation theory (CASSCF/NEVPT2) calculations, which provided the structure, thermodynamic stability, and EPR parameters of [Co(bdhb)$(py)_x$] complexes in their lowest Gibbs free energy conformers.

2. RESULTS AND DISCUSSION

2.1 Synthesis

The tetraketone H_2bdhb (Scheme 1) was first synthesized in 1977 by Alberts and Cram,[5,10] who also proposed its ring closure to yield a symmetric macrocyclic analogue, and subsequently by Yamamura *et al.*[6–8] with unspecified modifications. Thus, we directly followed the procedure outlined by the former authors, streamlining the purification process while still achieving a respectable final yield (72% compared to 81%). Briefly, deprotonation of acetylacetone (Hacac) at the methylenic and methyl positions was sequentially accomplished using NaH and *n*-BuLi, respectively, in dry THF at 0 °C. Nucleophilic attack of the resulting dianion on 1,3-bis(bromomethyl)benzene (3:1 molar ratio) in dry THF at 0 °C and then at room temperature (RT) was followed by standard acid work-up with final removal of all volatiles (including excess Hacac) to afford crude H_2bdhb. At this stage, Alberts and Cram utilized a rather involved, four-step purification procedure entailing a pre-purification by column chromatography followed by treatment with $Co(OAc)_2$ in methanol and isolation of the cobalt(II) complex as a pink solid. The pro-ligand was recovered by acid demetallation before a final purification by gel-permeation chromatography, which yielded H_2bdhb as a colorless oil. We found that a simple gradient flash chromatography run (silica gel, CH_2Cl_2/acetone eluent) afforded spectroscopically pure H_2bdhb as a light red oil in a single purification step.

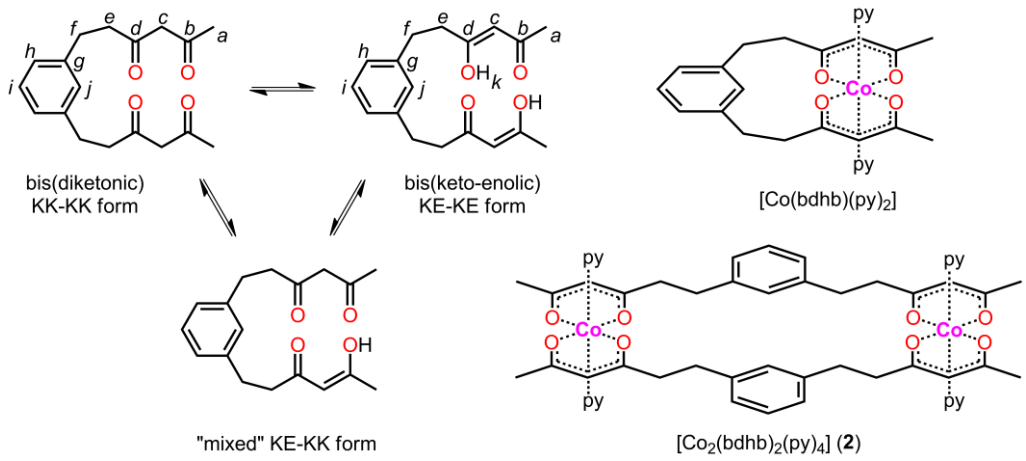

Scheme 1. Structures of the different tautomers of H_2bdhb, with the atom labelling scheme used in the discussion of NMR spectra, and of the monomeric $[Co(bdhb)(py)_2]$ and dimeric $[Co_2(bdhb)_2(py)_4]$ (**2**) complexes.

The spectroscopic characterization of H_2bdhb by NMR posed severe challenges due to the presence of keto-enol tautomerism, which generates multiple species in solution. In fact, each branch of the pro-ligand can be in either keto-enolic (KE) or diketonic (KK) form. By consequence, the H_2bdhb molecule can be found in bis(keto-enolic) form (KE-KE), in bis(diketonic) form (KK-KK),

or in a possible "mixed" form (KE-KK), featuring one keto-enolic and one diketonic branch (Scheme 1). Furthermore, the proportion of each form is expected to be solvent dependent.

Improving over previous work,[5–7] we carried out a comprehensive NMR characterization in acetone-d_6, as this solvent provided the best resolved spectra. The ^{1}H and ^{13}C NMR 1D spectra were complemented by 2D experiments like ^{1}H–^{13}C Edited Heteronuclear Single Quantum Coherence (E-HSQC), ^{1}H–^{13}C Heteronuclear Multiple-Bond Correlation (HMBC), and ^{1}H–^{1}H Correlated Spectroscopy (COSY), with cross-validation of data. These 2D experiments were an essential aid for assigning ^{1}H and ^{13}C resonances, as detailed in the Supplementary Note 1.

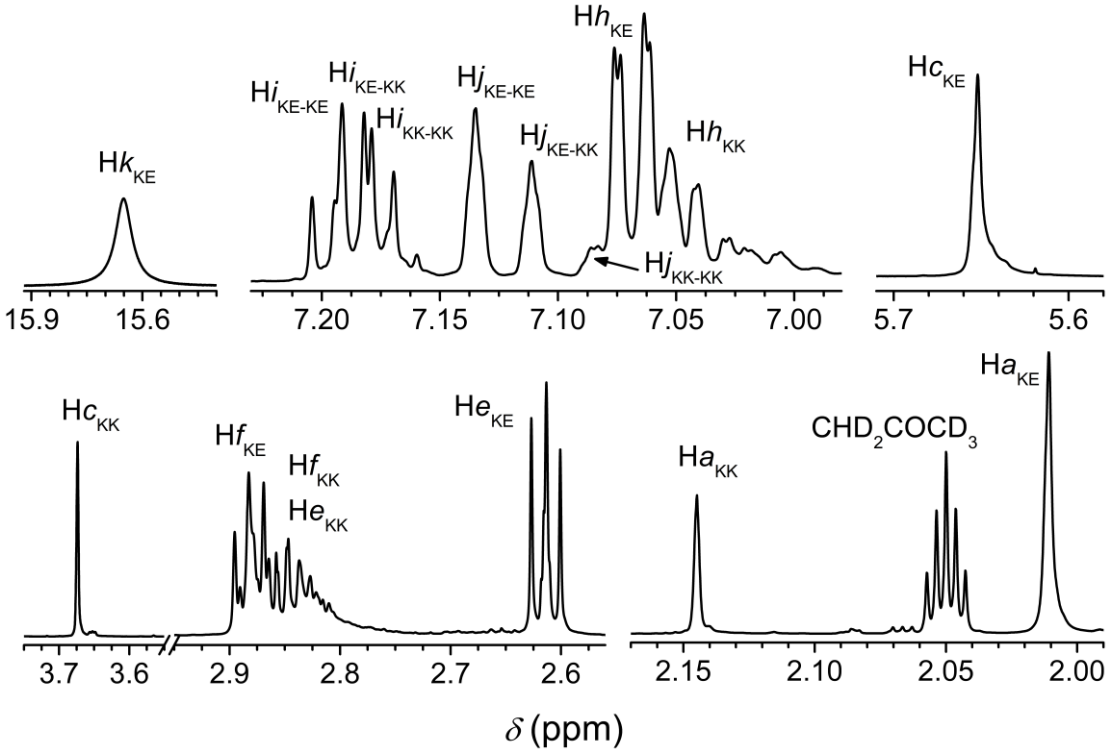

Figure 1. ^{1}H NMR spectrum of H_2bdhb in acetone-d_6 (600.13 MHz, 298 K), showing the assignment based on the labelling scheme of Scheme 1; the subscript in the peak label indicates the tautomeric form of the *proximal* branch (KE or KK) except for signals H*i* and H*j*, which are assigned specifically to KE-KE, KE-KK or KK-KK tautomers; processing parameters (TopSpin 4.3.0[11]): SI = TD, LB = 0.30 Hz. The water signal is hidden under the multiplet between 2.9 and 2.8 ppm.

In the ^{1}H NMR spectrum (Figure 1), the singlets at 3.67 and 5.65 ppm are typical of the CH_2 and CH groups of β-diketones in their diketonic and keto-enolic forms, respectively.[12–14] They were thus firmly assigned to the H*c* protons of the KK and KE branches, respectively (see Scheme 1 for the labelling scheme). Consistent with this, H*a* methyl protons also give two distinct resonances at 2.01 (KE) and 2.14 ppm (KK). The broad signal of the KE hydroxyl proton (H*k*) is observed at 15.65 ppm. Turning now to the protons of the dimethylene units (H*e* and H*f*), the pseudo-triplet at 2.61 ppm arises

from the H*e* protons of the KE branches, whereas the multiplet in the range of 2.9–2.8 ppm has overlapping contributions from the H*e* protons of the KK moieties and from the H*f* protons of both tautomeric branches. The chemical shift interval from 6.9 to 7.2 ppm contains a complex pattern of resonances arising from aromatic protons (H*h*, H*j*, H*i* in order of increasing δ).

Table 1. Experimental percentages of keto-enolic (KE) and diketonic (KK) branches of H_2bdhb and calculated percentages of the three tautomeric forms in Scheme 1 in different solvents at 298 K.

Solvent	%KE[a]	%KK[a]	%KE-KE[b]	%KE-KK[b]	%KK-KK[b]
acetone-d_6	74	26	55	38	7
dimethylsulfoxide-d_6	52	48	27	50	23
THF-d_8	86	14	74	24	2
CD_2Cl_2	78	22	61	34	5
$CDCl_3$[c]	84	16	71	27	2

[a]Evaluated from the relative areas of Ha_{KE} and Ha_{KK} signals. [b]Calculated assuming a statistical distribution of KE and KK branches in each molecule. [c]Alberts and Cram wrote[5,10] that H_2bdhb is completely in the enolic form in $CDCl_3$ at 40 °C; we found clear evidence of the diketonic moieties in both acetone-d_6 and $CDCl_3$ at 40 °C, with no significant variation down to 25°C; the observation of both KE and KK branches in $CDCl_3$ at 25 °C was also described by Yamamura *et al.*[6,7]

From the relative areas of the two H*a* components (Ha_{KE} and Ha_{KK}), the proportion of KE and KK branches in acetone-d_6 is 74:26. If a statistical distribution is followed, the KE-KE, KE-KK, and KK-KK tautomeric forms should occur in 55:38:7 proportion (Table 1), i.e. KE-KE and KE-KK should be the dominant tautomers.

The ^{13}C NMR spectrum (Figure 2) is consistent with this picture and contains 20 main signals, some of which are clearly split. Two main signals are observed for each carbon atom from C*a* to C*f*, consistent with the presence of both KE and KK branches. Two main signals are also detected for C*g* and C*h*, suggesting that the chemical shift of these aromatic carbons is mainly sensitive to the tautomeric form shown by the *proximal* branch. In support of this interpretation, the intensity ratio of the two components of both C*g* and C*h* is 74:26, and perfectly mirrors the proportion of KE and KK branches. Finally, C*i* and C*j* also afford two main resonances each, whose relative intensity is similar to that observed for the two well-separated H*j* pseudo-singlets at 7.14 and 7.11 ppm (Figure 1). These nuclei are in fact positioned on a molecular twofold axis and their relative intensity directly reflects the proportion of the dominant KE-KE and KE-KK forms.

The presence of a third tautomeric form (KK-KK) in minor amounts is evident upon closer inspection of the spectra. Both C*i* and C*j* afford an additional, upfield-shifted and much weaker resonance attributed to the KK-KK tautomer (Figure 2). Using the relative intensity of the three components of C*i* and C*j*, the calculated ratio between the KE-KE, KE-KK, and KK-KK forms is 55:39:6 and 51:41:8, respectively, and closely matches the statistical estimate in Table 1. Notice that

the H*j* signal of the KK-KK tautomer is also positioned upfield with respect to those of the dominant tautomers and is partially hidden by the neighboring H*h* multiplet (Figure 1), as proved by 2D experiments (see Supplementary Note 1).

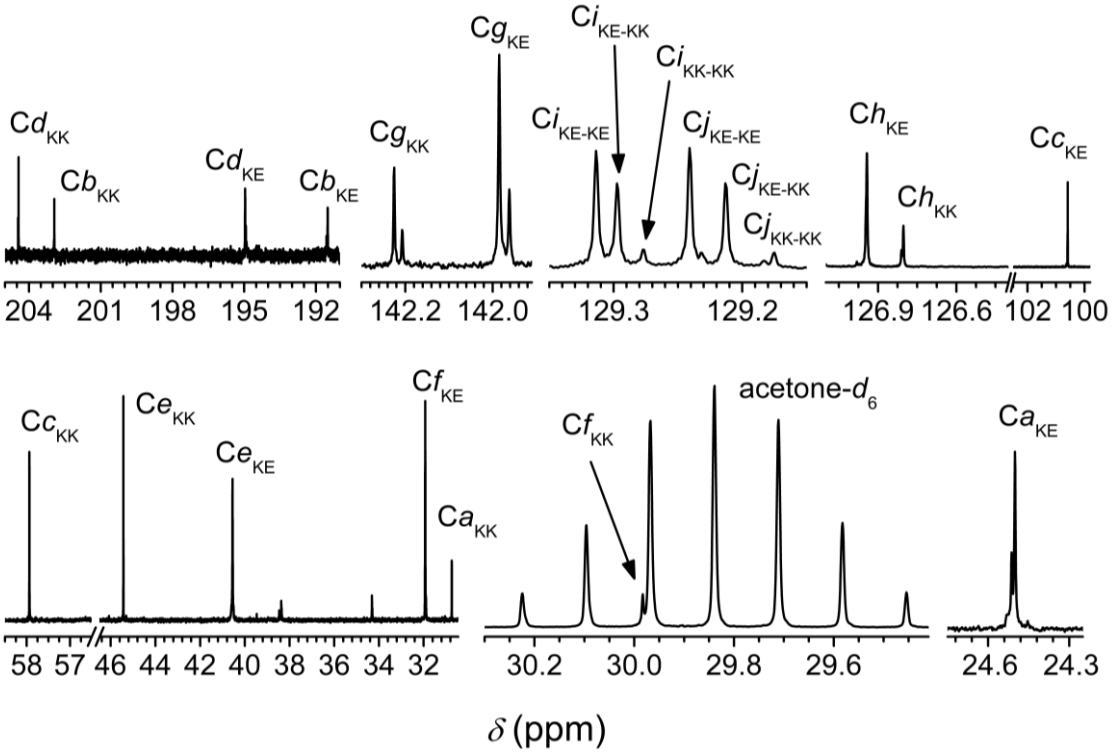

Figure 2. ^{13}C NMR spectrum of H_2bdhb in acetone-d_6 (150.90 MHz, 298 K), showing the assignment based on the labelling scheme of Scheme 1; the subscript in the peak label indicates the tautomeric form of the *proximal* branch (KE or KK) except for signals C*i* and C*j*, which are assigned specifically to KE-KE, KE-KK or KK-KK tautomers; processing parameters (TopSpin 4.3.0[11]): SI = 2·TD, LB = 0.30 Hz.

Other ^{13}C signals (*e.g.* Ca_{KE}, Ca_{KK}, Cb_{KE}, Cb_{KK}, Cc_{KE}, Cg_{KE}, Cg_{KK}, Ch_{KK}) are more or less evidently split, suggesting an effect from the *distal* branch. For instance, both Cg_{KE} and Cg_{KK} show a clear splitting into two components with markedly unequal intensity (Figure S1). This suggests that the C*g* nuclei of KE and KK branches have slightly different chemical shifts when they belong to the symmetric (KE-KE and KK-KK) or unsymmetric (KE-KK) forms. The proportion of the three tautomers calculated from the observed integrated intensities is 56:37:7 and is in very good agreement with the data in Table 1. Note that such splittings were in general more difficult to resolve in the ^{1}H spectra (see Supplementary Note 1).

The ^{1}H NMR spectra recorded in other solvents (dimethylsulfoxide-d_6, THF-d_8, CD_2Cl_2, and $CDCl_3$) gave different percentages of KE and KK branches and, by consequence, different calculated proportions of the three tautomeric forms (Table 1).

Alberts and Cram prepared a cobalt(II) complex of $bdhb^{2-}$ in their multi-step route to purify H_2bdhb, but provided no characterization data.[5] Following the same procedure, H_2bdhb and $Co(OAc)_2$ were combined in dry methanol, resulting in the immediate formation of a flocculent pink precipitate. The vacuum-dried solid is a pale pink powder (**1**) with composition $Co(bdhb)(H_2O)_2$, as established by combustion analysis and IR spectroscopy, soluble in THF but insoluble in MeOH, CH_2Cl_2, Et_2O, and *n*-hexane. Water molecules are clearly adventitious and may originate from solvents or contact with air moisture during filtration and washing operations. In this complex, the cobalt(II) ion is expected to exhibit an octahedral coordination geometry, with the four equatorial positions occupied by oxygen donors from the $bdhb^{2-}$ ligand, and the two axial positions occupied by water molecules.[15–17] Since $[Co(acac)_2(THF)_2]$ is a known crystalline compound,[18] we attempted to obtain crystalline samples by slow evaporation or cooling of a THF solution, as well as by solvent diffusion, without success. We then sought to aid crystallization by introducing ancillary ligands known to give adducts with $[Co(acac)_2]$, like alcohols,[19] DMF[20], and pyridine.[21–30] All attempts using various combinations of solvents and diffusion techniques failed, except with pyridine. X-ray quality orange-red crystals with composition $Co(bdhb)(py)_2$ were obtained by layering a THF solution of **1** with *n*-hexane or Et_2O containing 10% v/v of pyridine (Figure S11). Vapor diffusion of Et_2O into a THF solution of **1** containing a 4.5-fold molar excess of pyridine proved convenient for producing larger quantities of the compound, although it yielded material of lower crystalline quality. X-ray diffraction proved that the compound contains octahedrally coordinated cobalt(II) ions with two *trans* py ligands, but has a dimeric structure, i.e. $[Co_2(bdhb)_2(py)_4]$ (**2**).

2.2 X-ray Crystallography

A single-crystal X-ray diffraction experiment was successfully carried out on **2** at RT (Table S1 and Figure S12). Selected interatomic distances and interbond angles are gathered in Table 2. The compound is unexpectedly dimeric and centrosymmetric (Figure 3), with the two crystallographically equivalent cobalt(II) ions more than 11 Å apart from each other. The coordination environment is tetragonally elongated octahedral and consists of a *trans*-O_4N_2 donor set, with the O and N donors provided by the β-diketonato moieties of two different $bdhb^{2-}$ ligands and by the py molecules, respectively. It is therefore similar to that found in $[Co(acac)_2(py)_2]$ (**3**),[21] a well-known compound which will serve as a general reference for the structural and spectroscopic properties of **2**. Bond distances with β-diketonato and py donors are in the range 2.04-2.06 Å and 2.17-2.18 Å, respectively, and are consistent with a +2 oxidation state for the metal (Table S2).[31]

Cis O-Co1-O and N-Co1-O angles are 88.5-92.6° and 86.9-92.6°, respectively, while N1-Co1-N2 is 178.54(5)°. The four O donors bound to Co1 (O1, O2, O3′, O4′) are approximately on the same plane (rms dev.: 0.057 Å). Co1 lies almost exactly on that plane (dev.: 0.0267(6) Å), whereas Co1′ is displaced by 0.362(5) Å; this shows that the equatorial coordination planes of Co1 and Co1′, while parallel by symmetry, are significantly shifted from one another.

The dimethylene bridges display an *anti* conformation with torsion angles of 173-176° which position the 1,3-phenylene groups on opposite sides of the average plane through the β-diketonato moieties (Figure 3). The py ligands bound to the same metal ion are almost perpendicular to each other (80.30(6)°), while they are exactly orthogonal and parallel in the orthorhombic[21] and monoclinic[21,26] forms of **3**, respectively. The molecule has a wide central pore which hosts a py ring from a neighboring dimer (Figure S13).

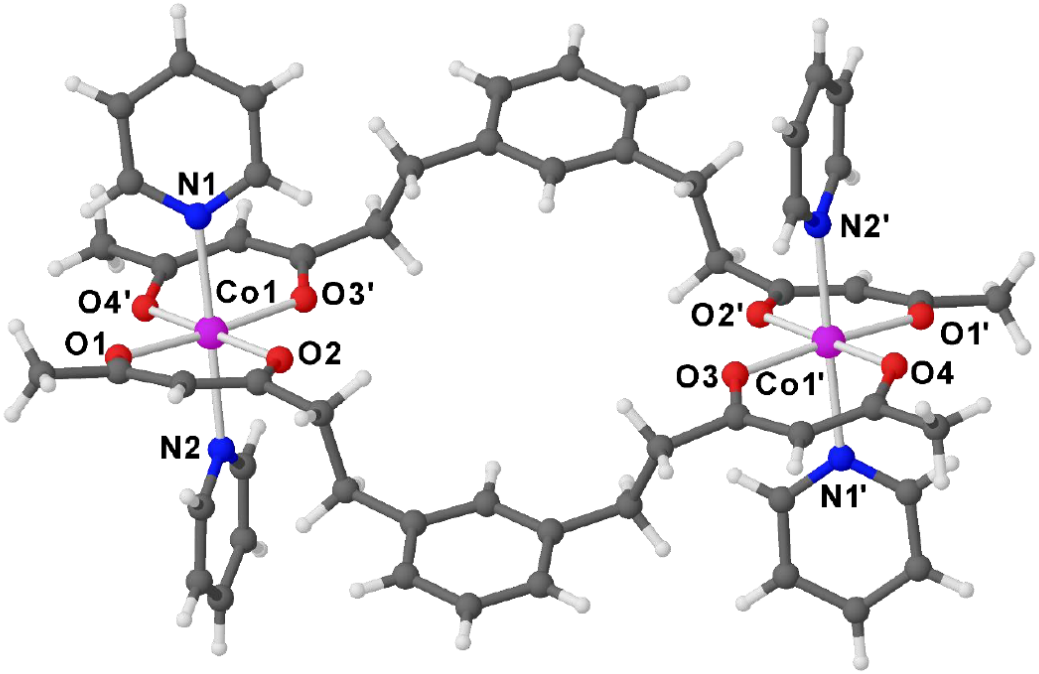

Figure 3. Ball-and-stick drawing of dicobalt(II) complex **2**, with the atom labelling scheme (Color code: C = dark gray, H = white, O = red, N = blue, Co = magenta). Primed atoms are related to unprimed ones by inversion through the center of the molecule. The rotational disorder of methyl groups is omitted.

Table 2. Selected interatomic distances (Å) and interbond angles (°) in **2**, with estimated standard deviations in parentheses.

Co1–O1	2.0492(10)	Co1–O2	2.0453(11)	Co1–O3′	2.0450(10)
Co1–O4′	2.0613(11)	Co1–N1	2.1695(13)	Co1–N2	2.1830(13)
Co1···Co1′	11.0694(5)				
N1–Co1–O1	86.94(5)	N1–Co1–O2	92.56(5)	N1–Co1–O3′	88.40(5)
N1–Co1–O4′	89.16(5)	N2–Co1–O1	92.50(5)	N2–Co1–O2	88.77(5)
N2–Co1–O3′	92.19(5)	N2–Co1–O4′	89.52(5)	O1–Co1–O2	89.14(4)
O2–Co1–O3′	89.90(4)	O3′–Co1–O4′	88.46(4)	O4′–Co1–O1	92.64(4)
O3′–Co1–O1	175.20(4)	O2–Co1–O4′	177.59(4)	N1–Co1–N2	178.54(5)

2.3 Solid-state studies

IR and UV-Vis-NIR spectroscopies. The FT-IR spectra of H_2bdhb, **1**, and **2** are compared in Figures S14 and S15. Compound **1** exhibits a broad OH stretching band centered around 3300 cm^{-1}, which is absent in **2** and confirms the presence of water. The intense bands of the pro-ligand between 1724 and 1587 cm^{-1} (C=O and C=C stretching) undergo a red shift of approximately 100 cm^{-1} upon coordination. The *in-plane* and *out-of-plane* bending bands of the pyridine ring, reported to occur at 626 and 432 cm^{-1} in **3**,[25] are observed at 624 and 431 cm^{-1} in **2** and are of course absent in **1**. The same spectral region features Co^{II}-O stretching bands (559 and 413 cm^{-1} in **3**,[25] 565 and 425 cm^{-1} in **1**, and 554 and 419 cm^{-1} in **2**).

The UV-Vis-NIR reflectance spectrum of **2** (Figure S16) has three main bands at 1020, 630 and 544-470 nm (structured), which mirror those observed in solid **3**[26,27] and are assigned to the $^4T_{1g}(F)\rightarrow{}^4T_{2g}$, $^4T_{1g}(F)\rightarrow{}^4A_{2g}$, and $^4T_{1g}(F)\rightarrow{}^4T_{1g}(P)$, ^2P, ^2G transitions of pseudo-octahedrally coordinated high-spin cobalt(II).[27,32]

Direct-current (DC) magnetic measurements. $\chi_M T$ vs. T and M_M vs. H curves of compound **2** are displayed in Figure 4 (χ_M and M_M are the molar magnetic susceptibility and the molar magnetization, respectively). $\chi_M T$ decreases with cooling from the RT value of 5.47 emu K mol^{-1}, which is higher than calculated for two noninteracting $S = 3/2$ centers taking $g = 2.00$ (3.75 emu K mol^{-1}). This result cannot be due to ferromagnetic coupling between the two cobalt(II) ions, as they are more than 11 Å apart from each other. Instead, it arises from a substantial orbital contribution to the magnetic moment, as in the structurally related dicobalt(II) complex $[Co_2(HL')_2(py)_4]$ described by Aromí *et al.* (H_3L' = 1,3-bis-(3-oxo-3-phenyl-propionyl)-2-hydroxy-5-methylbenzene; Co···Co = 7.955(1) Å).[33]

The electronic structure of tetragonally distorted octahedral high-spin cobalt(II) complexes like **3** and its 6-methylquinoline analogue has been investigated in great detail.[34] The ground electronic term ($^4T_{1g}$) of the octahedral complex splits into $^4A_{2g}$ and ^4E_g terms upon symmetry lowering. The former is the ground term and is further split by spin-orbit coupling (SOC) into two Kramers doublets (KDs). The effects of the low-symmetry distortion, SOC, and the interaction with the magnetic field are conveniently described by the so-called Griffith-Figgis Hamiltonian, which exploits the isomorphism between a P term ($L = 1$) and the octahedral orbital triplet T_{1g}:

$$\hat{H} = A\kappa\lambda\hat{\mathbf{L}}\cdot\hat{\mathbf{S}} + 3B_2^0(A\kappa)^2\left[\hat{L}_z^2 - \frac{1}{3}L(L+1)\right] + \mu_B(A\kappa\hat{\mathbf{L}} + g_e\hat{\mathbf{S}})\cdot\mathbf{B} \qquad (1)$$

In Eq. (1), $\hat{\mathbf{L}}$ and $\hat{\mathbf{S}}$ are the total orbital momentum and total spin momentum operators, respectively ($L = 1$ and $S = 3/2$), $\hat{L}_z$ is the operator associated with the component of **L** along the distortion axis z, λ is the SOC constant (taken to coincide with the value found in the ground Russell-Saunders term of the free ion, i.e. -171.5 cm^{-1}), B_2^0 is an axial parameter that quantifies the tetragonal distortion, μ_B is Bohr magneton, **B** is the applied magnetic field, and g_e is the free-electron g-factor. The κ coefficient is an orbital reduction factor accounting for metal-ligand bond covalency ($0 \le \kappa \le 1$). Typical reported values for bis(acetylacetonato) complexes of hexacoordinated cobalt(II) are 0.81-0.85.[34] The A coefficient, required by T-P isomorphism, takes the values $-3/2$ and -1 in the weak and strong crystal field limits, respectively.[35] For simplicity, we fixed $A\kappa$ at -1.2,[33] which corresponds to $\kappa = 0.8$ in the weak field limit. All DC magnetic data were then simultaneously fitted using PHI software[36] to give $B_2^0 = 159.5(14)$ cm^{-1} (Figure 4a). Treating $A\kappa$ as a second adjustable parameter gave $B_2^0 = 151.7(11)$ cm^{-1}, $A\kappa = -1.171(3)$, and an only slightly superior fit.

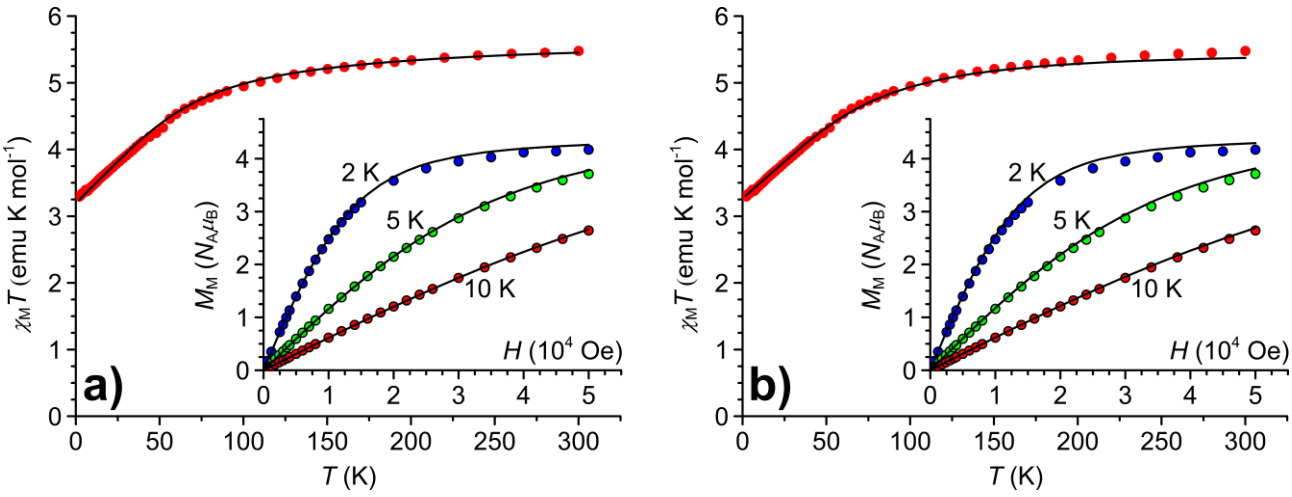

Figure 4. $\chi_M T$ vs. T curve measured on a polycrystalline sample of **2** (main panels) and M_M vs. H data collected at 2, 5, and 10 K on the same sample (insets). The solid lines provide the best fit to the experimental data using

Griffith-Figgis Hamiltonian in Eq. (1) (a) or single-ion spin Hamiltonian in Eq. (2) (b). N_A is Avogadro's constant and μ_B is Bohr magneton.

An attempt to add a rhombic crystal field term (B_2^2) to Eq. (1) led to only a marginal improvement of fit quality with a similar value for B_2^0 (160.0(11) cm^{-1}) and B_2^2 = 24(10) cm^{-1}, indicating a small rhombicity. The twelve energy levels resulting from Eq. (1) with $A\kappa = -1.2$ and B_2^0 = 159.5 cm^{-1} are displayed in Figure S17, along with their evolution when a magnetic field is applied along z or orthogonal to z. The two energetically lowest-lying KDs ($^4A_{2g}$ parentage) are split by ca. 140 cm^{-1} and are well separated from the upper levels (^4E_g parentage). Furthermore, their in-field evolution indicates an easy-plane (or hard-axis) anisotropy, the lowest-lying levels opening up faster for fields applied in the xy plane rather than along the z axis. Therefore, they can be mapped onto an S = 3/2 spin Hamiltonian (SH) with a positive axial zero-field splitting (ZFS) parameter D:

$$\widehat{H}_{\mathrm{ZFS}} = D\left[\hat{S}_z^2 - \frac{1}{3}S(S+1)\right] + E\left(\hat{S}_x^2 - \hat{S}_y^2\right) + \mu_B \mathbf{B}\cdot\mathbf{g}\cdot\hat{\mathbf{S}} \qquad (2)$$

where $\hat{S}_x$, $\hat{S}_y$, and $\hat{S}_z$ are the operators associated with the three cartesian components of **S** and **g** is the g-tensor for the S = 3/2 state. Setting the rhombic ZFS parameter E to zero to model a purely axial distortion and assuming an isotropic **g**, the DC magnetic data could be accurately fitted with D = 68.9(5) cm^{-1} and g_{iso} = 2.4103(12) (Figure 4b).

Alternating-current (AC) magnetic measurements. Magnetic measurements in AC mode showed that **2** displays detectable SMR in an external DC field (H_{DC}). In Figures S18-S20 we present the in-phase (χ'_M) and out-of-phase (χ''_M) components of molar magnetic susceptibility recorded as functions of frequency (ν) at different H_{DC} and T values. At a given H_{DC}, the maximum of the χ''_M vs. ν curve shifts towards lower frequencies with decreasing temperature, a behavior consistent with that observed in other cobalt(II) β-diketonates.[17]

While SMR is normally associated with an easy-axis magnetic anisotropy ($D < 0$ in Eq. (2)),[37] high-spin cobalt(II) complexes may exhibit SMR even when their anisotropy is of the easy-plane type. This behavior is known for coordination numbers three,[38] four,[39–42] five,[43–48] six,[17,49–60] and seven[61–63] and is only observable under an applied DC field. The reason is intimately related to the Kramers character of cobalt(II) ground state and was explained by some of us in a previous work on pseudo-octahedral [Co(acac)$_2$(H$_2$O)$_2$].[17] Although in a classical picture an easy-plane system with some in-plane anisotropy might experience an energy barrier to magnetic moment reversal, SMR in easy-plane cobalt(II) complexes was shown to originate from combined direct and Raman mechanisms. The former dominates at very low temperature and would be forbidden by Kramers theorem in zero field, but becomes allowed through hyperfine interaction with the I = 7/2 nucleus of

^{59}Co (natural abundance = 100%). However, it is impossible to detect SMR in zero DC field, since transitions between electronuclear spin states yield vanishingly small magnetic moment changes. Once an external DC field is applied, each state gains a measurable magnetic moment, thus making transitions between them detectable by magnetic susceptibility measurements.

The χ'_M vs. ν and χ''_M vs. ν curves were fitted by using the method described in Supplementary Note 2 to investigate the dependence of the magnetization relaxation time (τ) on H_{DC} and T (Figures S18-S20).[64] The best-fit parameters are gathered in Tables S3-S5, while their plots as a function of H_{DC} and T are reported in Figures 5 and S21-S23. The temperature dependence of τ at H_{DC} = 3000 Oe is presented in Figure 5a. The relaxation time shows a reduced temperature dependence in the 2-3 K range, while it drops rapidly above 3 K. Such a behavior is well-reproduced by a model accounting for one-phonon (direct) and two-phonon (Raman) relaxation processes, as described by Eq. (3):[65]

$$\tau^{-1}(T) = a_{\mathrm{dir}}T + a_{\mathrm{Ram}}T^{n} \qquad (3)$$

In the above equation, a_{dir} and a_{Ram} are two scaling factors for the direct and Raman processes, respectively, and n is a phenomenological parameter ranging from 2 to 9 depending on the system.[65–67] The best-fit parameters are a_{dir} = 836(17) K^{-1} Hz, a_{Ram} = 0.4(1) K^{-n} Hz, and n = 6.3(2) (blue curve in Figure 5a). These values compare well with those previously reported for other high-spin cobalt(II) complexes with $D > 0$.[61,68,69]

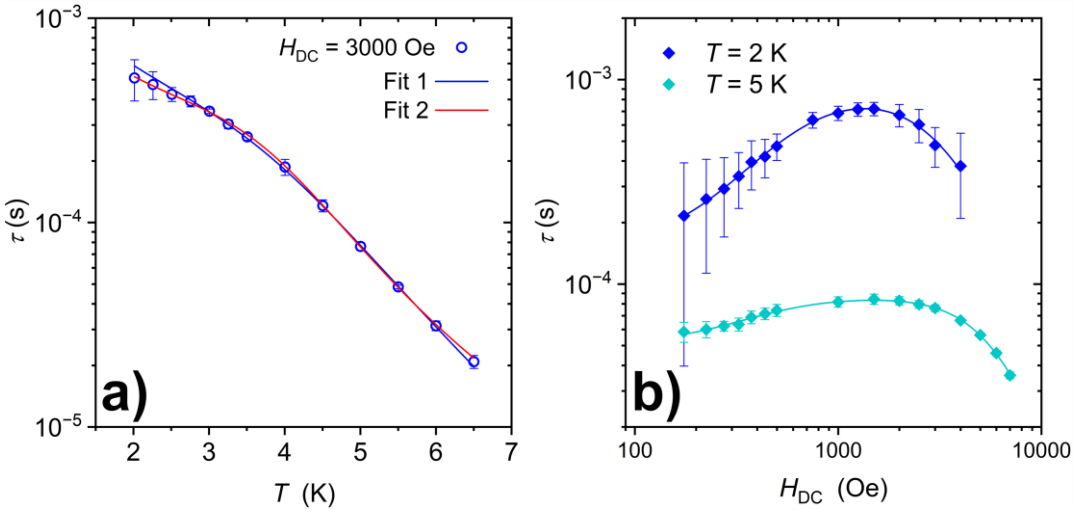

Figure 5. (a) τ vs. T data for **2** recorded at H_{DC} = 3000 Oe. Overlayed blue and red lines represent the best-fit curves obtained using Eqs. (3) and (4), respectively. (b) τ vs. H_{DC} data for **2** recorded at 2 and 5 K, together with the best-fit curves obtained using BVV model in Eq. (5) with the parameters reported in Table 3. The error bars on τ values are larger at 2 K than at 5 K because of the wider distribution of relaxation times.

For some of these complexes, a fitting of the high-temperature τ vs. T data to an Arrhenius law, i.e. $\tau^{-1} = \tau_0^{-1}\exp\left(-U_{eff}/k_{\mathrm{B}}T\right)$, as appropriate for a dominant Orbach relaxation process, yielded an effective relaxation barrier U_{eff} close to the energy gap between the two KDs of the zero-field split $S = 3/2$ state ($\approx 2D$).[39] In our case, the effective barrier obtained by the same fitting procedure (U_{eff} = 11.1(7) cm^{-1}, see Figure S24) is much lower than $2D$ and is clearly incompatible with the electronic structure of **2**, confirming our hypothesis that relaxation occurs via direct and Raman processes.

Since Eq. (3) offers little insight into the microscopic origin of the relaxation mechanisms involved, we also used a model better suited to provide a physical explanation of the temperature dependence of magnetization dynamics for (effective) S = ½ systems (the ground KD can be treated as an effective S' = ½ spin):[70–74]

$$\tau^{-1}(T) = a_{\mathrm{dir}}\frac{e^{\Delta_1/k_{\mathrm{B}}T}}{e^{\Delta_1/k_{\mathrm{B}}T}-1} + a_{\mathrm{Ram}}\frac{e^{\Delta_2/k_{\mathrm{B}}T}}{\left(e^{\Delta_2/k_{\mathrm{B}}T}-1\right)^2} \qquad (4)$$

The first term in Eq. (4) accounts for the direct relaxation process, triggered by a phonon with energy Δ_1 matching the energy gap between the two $|m_{S'}\rangle = \pm 1/2$ states of the Zeeman-split ground KD. Considering H_{DC} = 3000 Oe and an isotropic g_{iso} = 2.41, the Δ_1 value was fixed to 0.34 cm^{-1}. The second term contains the Raman contribution to relaxation, which is caused by a phonon with energy Δ_2. Thus, the only fitting parameters are a_{dir}, a_{Ram}, and Δ_2. The best-fit curve (red curve in Figure 5a) is close to that obtained using Eq. (3) but is more effective in reproducing the experimental trend below 3 K. The best-fit parameters a_{dir} = 297(3) Hz, a_{Ram} = 6.6(7)·10^6 Hz, and Δ_2 = 23.1(4) cm^{-1} indicate a strong influence of low-energy phonon modes on the spin-lattice relaxation mechanism. We note, however, that these values only indicate potential phonon region modes affecting relaxation. In fact, additional higher- and lower-energy phonon modes could be required to fully capture the phonon-induced spin relaxation in **2**. A combined theoretical-experimental approach is hence needed to further validate this hypothesis.[75,76]

We also analyzed the magnetic field dependence of χ'_{M} and χ''_{M} and extracted the τ vs. H_{DC} curves at T = 2 and 5 K (Figure 5b). The relaxation time follows the general trend expected for a Kramers ion, with a low-field region where τ increases on increasing field (from 100 to 1500 Oe) followed by an abrupt decrease at higher fields. This can be explained by considering two distinct relaxation processes dominating in the two field regions. At low field, the increasing Zeeman splitting induced by the applied magnetic field overcomes both hyperfine and inter/intramolecular coupling interactions, causing a slowing down of relaxation. When the field is sufficiently large to override spin-spin and spin-nuclei interactions, any further increase in field only results in an increase of the Zeeman splitting of the ground KD. Correspondingly, there are more phonons matching the energy

difference between the two levels, and the direct relaxation mechanism becomes predominant. Based on these considerations, we fitted the τ vs. H_{DC} data using Eq. (5), derived from Brons-van Vleck (BVV) model,[73,77–79] whose parameters are temperature dependent:[80,81]

$$\tau^{-1}(H_{DC}) = c(H_{DC})^x + d\frac{1+e(H_{DC})^2}{1+f(H_{DC})^2} \quad (5)$$

The first term in Eq. (5) accounts for the direct relaxation mechanism, whose contribution is modulated by the *c* scaling factor. It usually increases with the fourth power of H_{DC} ($x = 4$), but in our treatment *x* was left free to vary in the range from 1 to 4. The second term accounts for the effect of spin-spin and spin-nuclei interactions. In particular, the *d* parameter corresponds to the zero-field relaxation rate triggered by internal fields, *e* accounts for the contribution of internal fields to the relaxation process, and *f* describes the efficiency of the external DC field in suppressing relaxation through these channels.[82] The best-fit parameters so obtained are collected in Table 3.

Table 3. Best-fit parameters for BVV model applied to τ vs. H_{DC} curves at 2 K and 5 K in Figure 5b.

	$T = 2$ K	$T = 5$ K
c (Hz Oe^{-x})	$8.8(3)\cdot10^{-9}$	$2.7(1)\cdot10^{-10}$
x	2.3(3)	2.8(1)
d (Hz)	7(1)	20(1)
e (Oe^{-2})	$3(1)\cdot10^{-6}$	$7(2)\cdot10^{-6}$
f (Oe^{-2})	$1.9(6)\cdot10^{-5}$	$1.1(3)\cdot10^{-5}$

Given the relatively small number of experimental points at high fields, we refrain from attaching a specific meaning to this reduced field dependence of direct relaxation at both temperatures ($x = 2.3$-2.8). A marked effect of BVV relaxation on magnetization dynamics is revealed by the increment of both *d* and *e* parameters passing from 2 to 5 K. This can be explained by considering that phonons are less effective in promoting relaxation at 2 K than at 5 K, due to the lower number of active phonons that match the difference in energy between the two spin levels. Hence, the application of a small magnetic field at 2 K leads to a fast suppression of the dynamics induced by internal fields. On increasing *T*, the probability of a phonon to match this energy splitting increases, and larger fields are necessary to suppress BVV relaxation.

EPR spectroscopy. A microcrystalline powder sample of **2** was measured by continuous wave (CW) X-band EPR spectroscopy at $T = 10$ K (see Experimental section for more details). The experimental spectrum, reported in Figure 6a, has the structure expected for a high-spin cobalt(II) ion in a distorted octahedral coordination environment. As discussed in the section on DC magnetic measurements, the ground state of the cobalt(II) ions is a spin quartet with an easy-plane magnetic anisotropy, which

positions the first-excited KD at ≈ $2D$ ≈ 140 cm^{-1} from the ground KD. Therefore, the observed broad bands at 50 – 250 mT and 260 – 420 mT arise from transitions within the ground KD. A substructure due to hyperfine coupling interaction between the electronic spin and the ^{59}Co nucleus (I = 7/2) cannot be perfectly resolved, but contributes to the final spectral shape.

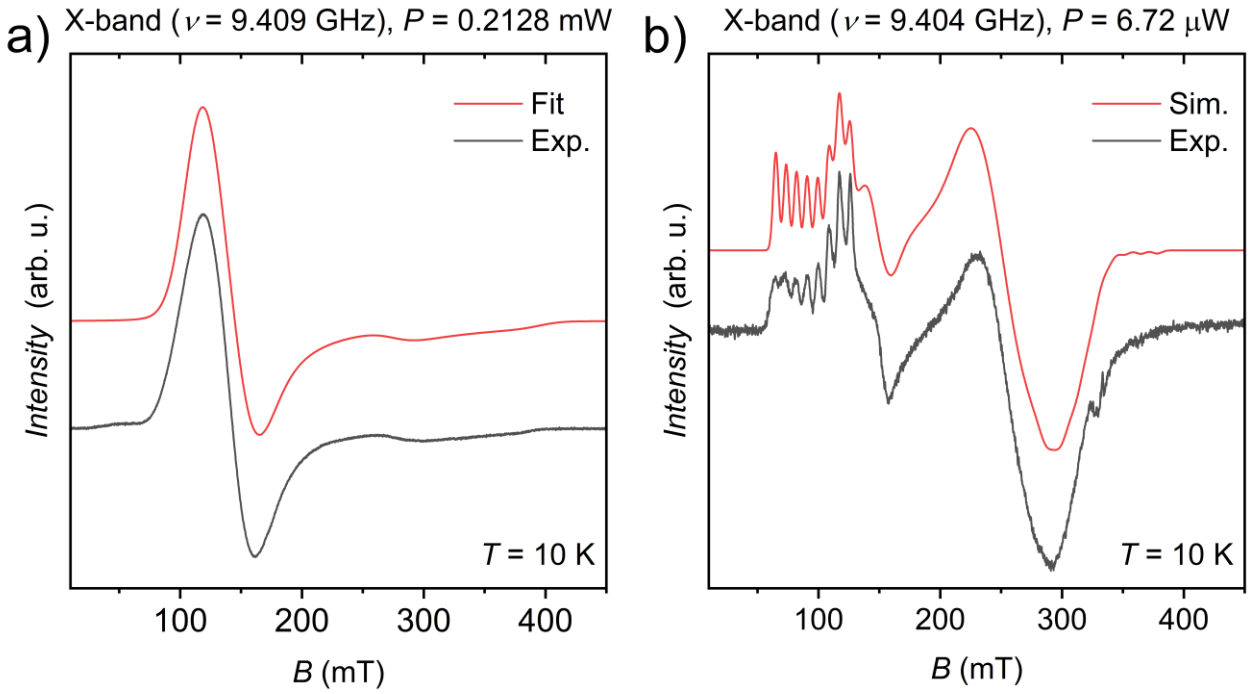

Figure 6. (a) CW X-band EPR spectrum of a microcrystalline powder sample of **2** and spectrum computed using the best-fit parameters reported in Table 4. (b) CW X-band EPR spectrum of a frozen 0.1 mM solution of **2** in CH_2Cl_2/toluene (1:1 v/v) and its simulation using the parameters reported in Table 4.

In this framework we simulated[83] the experimental data by considering the SH for an effective S' = 1/2 spin, as described by Eq. (6):

$$\widehat{\mathcal{H}}_{\mathrm{EPR}} = \mu_{\mathrm{B}}\mathbf{B}\cdot\mathbf{g}'\cdot\widehat{\mathbf{S}}' + \widehat{\mathbf{S}}'\cdot\mathbf{A}'\cdot\hat{\mathbf{I}} \qquad (6)$$

Here, the two terms account for the Zeeman and hyperfine coupling interaction, described by the effective interaction tensors **g'** and **A'**, respectively. A first set of simulation parameters (Table S6) providing the best visual agreement with the experimental spectrum (Figure S25) was obtained by manually varying the parameter values. The pattern of principal **g'** components ($g'_z \approx g_e < g'_y < g'_x$) is consistent with previous reports on cobalt(II) acetylacetonato adducts,[34] suggesting a considerable in-plane rhombicity. Although hyperfine coupling interaction can be added to correctly reproduce line shapes, the sizable anisotropic strain contribution to the linewidth (**Γ**) hampers a correct estimation of all the components. This strain can be ascribed to dipolar coupling interactions, defects, and unresolved hyperfine structures in the solid matrix. We stress here that strain strongly affects all components, limiting the accuracy on the estimation of A'_x and A'_y, but is not sufficient to justify the

broad shape of g'_z signal within the 260 – 420 mT range. Indeed, this signal can only be reproduced by considering A'_z = 400 MHz, which we hypothesize is greater than A'_x and A'_y. Such a quasi-axial **A'** anisotropy along the smaller principal component of **g'** has already been observed in tetrahedral cobalt(II) complexes with mixed sulfur-nitrogen chelating ligands.[84] To reach a more accurate estimation of A'_z and **Γ** components and their uncertainties, we further performed a fit by using a hybrid fitting protocol (see Supplementary Note 3) and setting $A'_x = A'_y = 0$ (i.e. attributing the linewidth to residual anisotropic broadening only). This provided the computed spectrum shown in Figure 6a and the best-fit parameters reported in Table 4.

Table 4. Best-simulation EPR parameters for **2** in powder and frozen solution samples at T = 10 K.[a]

	powder	frozen solution[b,c]	
		2A[d]	**2B**[d]
S'	1/2	1/2	1/2
g'_x	5.75[c]	5.65	2.30
g'_y	4.55[c]	4.45	2.57
g'_z	2.00[c]	2.01	6.98
A'_x (MHz)	0	145	280
A'_y (MHz)	0	145	300
A'_z (MHz)	422(3)[e]	420	850
Γ_x[f] (MHz)	2441(30)[e]	900	790
Γ_y[f] (MHz)	2268(21)[e]	850	1000
Γ_z[f] (MHz)	900(53)[e]	250	505

[a]Based on the effective SH in Eq. (6). [b]0.1 mM in CH_2Cl_2/toluene (1:1 v/v). [c]Parameters obtained by manual simulation of the spectra; as such, uncertainties on parameters cannot be determined. [d]**2A** and **2B** are the two spectral components detected in frozen solution. [e]Parameters providing the best fit to the spectrum using the protocol reported in Supplementary Note 3; standard deviations (in parentheses) were calculated as the square-root of the covariance matrix outcoming from the fit. [f]Components of anisotropic residual linewidth vector **Γ** = [Γ_x Γ_y Γ_z] for modeling linewidths; isotropic broadening was modeled with a pseudo-Voigtian line-shape of 2 mT for both Gaussian and Lorentzian contributions.

The observed rhombicity of the EPR spectrum can be in principle traced back to the principal g-factors (g_x, g_y, and g_z) and $E/D = \eta$ ratio in Eq. (2) by using the relations first reported by Pilbrow[85] for S = 3/2 and $D > 0$:

$$g'_x = g_x\left(1 + \frac{1-3\eta}{\sqrt{1+3\eta^2}}\right) \quad (7a)$$

$$g'_y = g_y\left(1 + \frac{1+3\eta}{\sqrt{1+3\eta^2}}\right) \quad (7b)$$

$$g'_z = g_z\left(1 - \frac{2}{\sqrt{1+3\eta^2}}\right) \quad (7c)$$

We might in principle use the isotropic g_{iso} value obtained by DC magnetometry to evaluate η, but this does not provide any solution in agreement with the $g'_{x,y,z}$ values determined by EPR. However, leaving the principal *g*-factors of the $S = 3/2$ state free to vary while constraining them to be axial and averaged at $g_{iso} = 2.41$ provides a very good solution for $\eta = \pm 0.078$, $g_x = g_y = 2.592$, and $g_z = 2.041$).

Computational studies. To gain more insight into the magnetic properties of **2**, multiconfigurational CASSCF/NEVPT2 calculations were performed (see Experimental section for details). The pattern of energetically low-lying KDs (Table S7) shows that the ground and first-excited KDs have an energy difference of 188 cm^{-1}, and are well separated from the next KDs (778 cm^{-1}). Although these calculated ZFS values are slightly larger than those obtained by fitting DC magnetic data with Eqs. (1) or (2) (see also Figure S17), they provide the same overall picture and, in particular, confirm that the system can be well described by a SH, like Eq. (2). It is known that the *D* value depends on the orbitals involved in the electronic excitations and the energy difference between them. The calculated *D* value in **2** is large and positive (93.6 cm^{-1}), in agreement with the experimental results. The positive *D* value in this distorted octahedral geometry indicates that the electronic excitations that contribute to such value are from the d_{xz} and d_{yz} orbitals to the d_{xy} orbital, involving an m_l change of ±1. The *ab-initio* ligand field theory (AILFT) analysis in Figure S26 corroborates such assumption showing that the d_{xz} and d_{yz} orbitals are the energetically lowest-lying doubly occupied orbitals and the d_{xy} orbital remains singly occupied. The rhombic ZFS parameter (*E*) is substantial although not very large (6.6 cm^{-1}) and the *E*/*D* ratio (η = 0.07) is in remarkable agreement with the value provided by the perturbative analysis based on Pilbrow's relations ($\eta = \pm 0.078$). It implies that the quantum tunneling of the magnetization will be significant, although the anisotropy of the complex can be described as easy plane.

The analysis of the **g'** tensor for the ground KD gave principal values $g'_x = 5.902$, $g'_y = 4.543$, and $g'_z = 2.123$, which describe an easy-plane anisotropy. The hard axis is directed along the N1-Co1-N2 direction while the easy plane lies close to the plane formed by the β-diketonato moieties (see Figure S27). By contrast, the first excited KD has an easy-axis character, with principal *g*-factors of 0.483, 0.688 and 5.423. In general, when comparing the calculated and experimental *D* and *g*-factors or, more directly, the simulated susceptibility and magnetization curves with the experimental ones (Figure S28), it can be observed that the parameters are overestimated by the calculation.

Additionally, the *ab initio* blocking barrier for **2** has been computed (Figure 7). The tunneling transition probabilities are very large, especially within the ground KD, which confirms the necessity of applying an external DC magnetic field for the observation of SMR. The transition probability for

the Orbach process is close to 0.1, so once an external DC magnetic field is applied, an energy barrier of more than 180 cm^{-1} is estimated. However, that is rarely the case in this type of complexes due to the presence of other relaxation processes not included in the calculations.

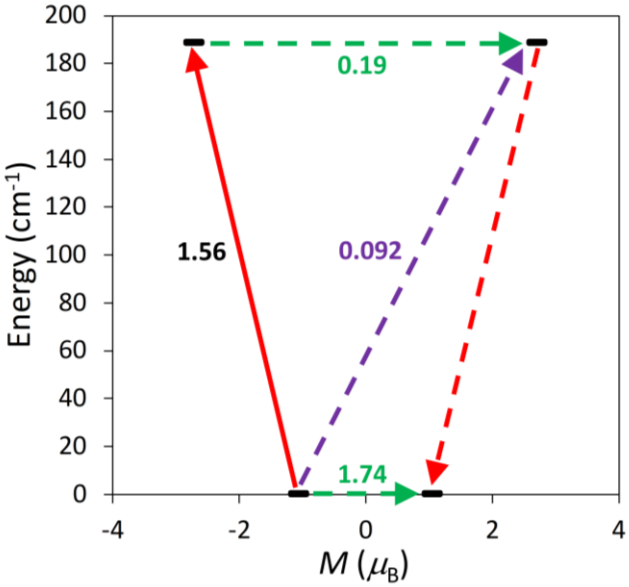

Figure 7. Calculated energies of the four states belonging to the first and second KDs as function of their average projected magnetic moment, and transition probabilities between states. Values above 0.1 indicate an efficient spin relaxation mechanism. The dashed green arrows correspond to the tunneling process, the dashed purple arrow shows the hypothetical Orbach relaxation process, and the red arrows indicate the transition between the ground and excited KDs (solid) and the relaxation pathway to the ground state with reversed spin (dashed).

2.4 Solution studies

UV-Vis-NIR spectroscopy. Compounds **1** and **2** are both soluble in THF, but only **2** is soluble in a non-coordinating solvent like CH_2Cl_2. The UV-Vis-NIR spectra of H_2bdhb, $bdhb^{2-}$, **1**, and **2** in THF are compared in Figures S29 and S30. The π→π* absorption of H_2bdhb at 274 nm shifts to 293 nm upon double deprotonation and is observed at 291 nm in **1** and **2**. Between 400 and 800 nm the spectra of the two cobalt(II) complexes are strikingly similar, suggesting that they both undergo solvolysis in THF. Most likely, this involves replacement of the H_2O and py ligands by solvent molecules, which also explains the good solubility of **1** in THF. Consistent with this interpretation, when an excess of pyridine is added to the solution, the spectrum undergoes remarkable changes, with an overall blue shift of the absorption bands, signalling an enhanced crystal-field splitting (Figure S30). The final set of bands is indeed similar to that found in pyridine solutions of **3** and hints at the formation of hexacoordinated complexes containing two py ligands.[86] Moving from THF to CH_2Cl_2, the electronic

absorption bands of **2** in the visible region shift to higher wavelengths by 20-25 nm (Figure S31 and S32). However, upon addition of excess pyridine the spectrum becomes identical to that recorded in the same conditions in THF (Figure S32). For consistency with EPR experiments (see below), a CH_2Cl_2/toluene (1:1 v/v) solvent mixture was also tested (Figure S33) and gave similar spectral features and the same response to the addition of excess pyridine as pure CH_2Cl_2. These data suggest that **2** undergoes significant dissociation of the py ligands in solution and that excess pyridine is required to restore hexacoordination, but they provide no insight into a possible structural rearrangement to give monomeric species.

Mass spectrometry. More informative on solution structures are the ESI-MS spectra recorded in positive-ion mode on **1** and **2** dissolved in THF. They are dominated by the signals of monomeric complexes $[Co(bdhb)]^+$ and $[Co(bdhb)(py)]^+$, respectively, with barely detectable or no peaks attributable to dimeric species (Figures S34 and S35). The spectrum of **1** in THF changes significantly after the addition of py (2:1 molar ratio to Co), whereupon $[Co(bdhb)(py)_2]^+$ gives the strongest signal (Figure S36). These results prove the ability of $bdhb^{2-}$ to coordinate with both branches to the same metal ion to give monomeric species and suggest that the solid-state dimeric structure of **2** is not fully preserved in solution, at least under ESI-MS ionization conditions.

Magnetic measurements and NMR spectroscopy. The magnetic properties of **2** in CD_2Cl_2 at 298 K were investigated by Evans method, which gave $\chi_M T$ = 5.2 emu K mol^{-1} per dicobalt(II) unit. The value is in close agreement with solid-state data (5.47 emu K mol^{-1} at 300 K) and shows that high-spin cobalt(II) ions persist in CD_2Cl_2 solution. The ^{1}H NMR spectrum of **2** collected in CD_2Cl_2 at 298 K shows many broad and partially overlapping peaks, some of which undergo considerable paramagnetic shifts (Figure 8). A comparison with the ^{1}H and ^{2}H NMR spectra of isotopically labelled compound $[Co_2(bdhb)_2(py\text{-}d_5)_4]$ (**2-*d*$_{20}$**) allowed to firmly assign the resonances at 53.9, 14.4, and −2.1 ppm to *o*-py, *m*-py, and *p*-py protons, respectively (Figures 8 and S37). This assignment is consistent with the ordering of paramagnetic shifts reported for **3** in $CDCl_3$[28,30] as well as with the observed width and relative area (~1.3 : 2 : 1) of the peaks (the intensity of the first signal is most probably affected by the proximity of *o*-py protons to the paramagnetic cobalt(II) center). It is then clear that the pyridine molecules are bonded to (or in fast exchange with) the metal ions and that the remaining, unassigned broad peaks in the spectrum arise from the coordinated $bdhb^{2-}$ ligand. Although the structured signal at 25-26 ppm matches the position of methyl proton resonances in halocarbon solutions of **3**,[24,29] we refrain here from proposing further assignments, since resolutive information was provided by ^{1}H DOSY experiments.

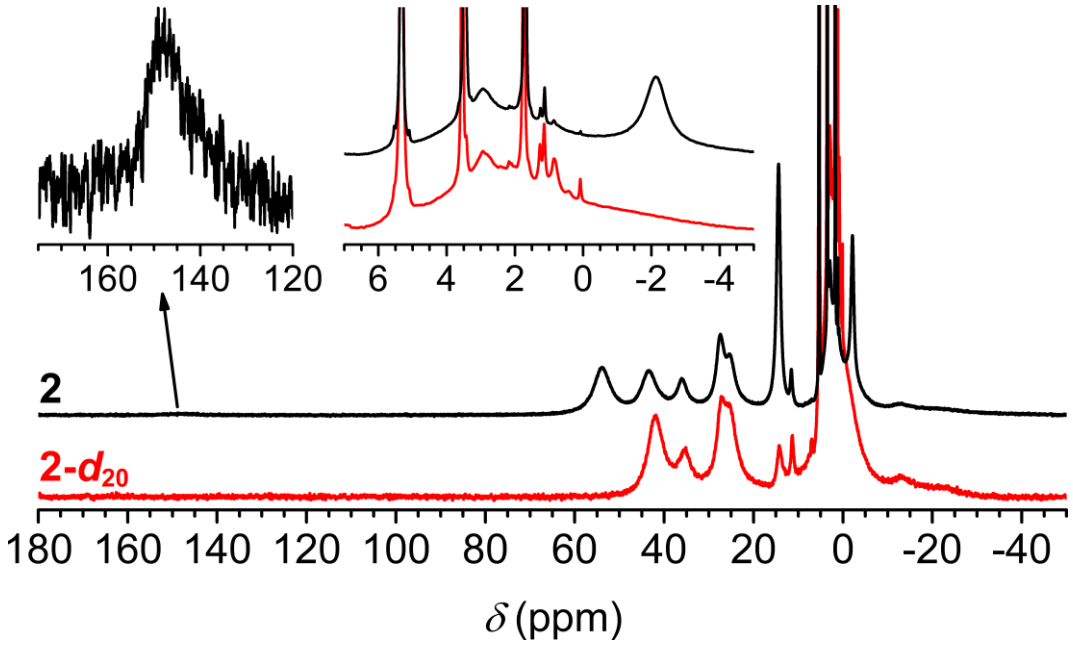

Figure 8. ^{1}H NMR spectrum of **2**/**2-*d*$_{20}$** in CD_2Cl_2 (400.13 MHz, 298 K); δ (ppm) = 5.32/5.32 (residual protons in CD_2Cl_2), 3.47/3.54 [m, THF, CH_2(2,5)], 3.41/3.43 (q, Et_2O, CH_2), 1.70/1.74 [m, THF, CH_2(3,4)], 1.26 (br, pump oil, CH_2), 1.13/1.14 (t, Et_2O, CH_3), 0.86 (br, pump oil, CH_3). Processing parameters [TopSpin 4.3.0[11]]: SI = TD, LB = 10.00 and 20.00 Hz for **2** and **2-*d*$_{20}$**, respectively. Residual THF and Et_2O presumably reflect an incomplete removal of the mother solution by vacuum treatment. The very weak resonance at ~147 ppm in the spectrum of **2** is not observed in the deuterated sample and most probably arises from an unknown impurity.

This powerful NMR-based method is used to estimate the molecular weight (*MW*) of species in solution by measuring their diffusion coefficient (*DC*).[87–89] The *MW* is related to the *DC* through the following power law:

$$DC = K \cdot MW^{\alpha} \qquad (8)$$

where K and α are empirical parameters obtained from external calibration curves (ECCs).[90,91] While the determination of *MW* by DOSY is routine for small organic molecules and polymers, successful applications of this technique to paramagnetic transition metal[9,92,93] or lanthanoid[94] complexes are rare, as DOSY analysis is extremely challenging or unfeasible when NMR resonances are broad or undergo large paramagnetic shifts.[92] We nevertheless attempted to employ the DOSY technique to clarify whether **2** undergoes a structural rearrangement from dimeric to monomeric in solution, as suggested by ESI-MS data. As expected,[92] only the four proton resonances lying between 14.4 and −2.1 ppm gave a measurable DOSY signal (Figure S38). The two peaks at 11.5 and 2.9 ppm exhibit similar associated *DC*s ($1.1 \cdot 10^{-9}$ m^2 s^{-1} after averaging and normalization) and originate from the slowest diffusing species present in solution, i.e. the cobalt(II) complexes of $bdhb^{2-}$. Remarkably, the free H_2bdhb pro-ligand has $DC = 1.2 \cdot 10^{-9}$ m^2 s^{-1} in CD_2Cl_2,[9] which suggests a similar size for H_2bdhb

and the cobalt(II) complexes, directly hinting at a monomeric structure for the latter. The *m*-py and *p*-py resonances at 14.4 and –2.1 ppm, respectively, also gave a measurable DOSY signal with similar associated *DC*s ($1.6 \cdot 10^{-9}$ m^2 s^{-1} after averaging and normalization). It follows that the py ligand diffuses faster than the cobalt(II) complexes of $bdhb^{2-}$, but slower than free pyridine in CD_2Cl_2 ($2.65 \cdot 10^{-9}$ m^2 s^{-1} after averaging and normalization), indicating a fast chemical exchange of py between coordinated and free forms. Assigning to coordinated py the same *DC* as the cobalt(II) complexes ($1.1 \cdot 10^{-9}$ m^2 s^{-1}) and using a weighted averaging procedure,[95] a 68:32 molar ratio is evaluated between coordinated and free py.

ECCs developed for organic molecules with *MW* up to ~600 g/mol in dichloromethane[91] were then used to estimate the *MW* of the cobalt(II) complexes. Two different ECCs were tested, namely ECC_{DSE} and ECC_{MERGE} of Ref. [91], which gave *MW* = 402±117 and 437±138 g mol^{-1}, respectively. Comparison with the calculated *MW*s for dimeric **2** and monomeric [Co(bdhb)$(py)_2$] (1034.96 and 517.48 g mol^{-1}, respectively) strongly suggests that **2** undergoes rearrangement to monomers in CD_2Cl_2 solution (Figure S39). The values provided by the DOSY experiment are 15-20% smaller than the *MW* of [Co(bdhb)$(py)_2$], although the difference lies barely within the error bar. A partial dissociation of the py ligands will certainly contribute to decreasing the apparent *MW* of the complexes (e.g. *MW* = 470.02 g mol^{-1} for [Co(bdhb)$(py)_{1.4}$]). It is also known that ECCs based on light-atom molecules can afford underestimated *MW*s for heavy atom derivatives,[92,96] whose molecular density is higher than that of the reference molecules. Therefore, we tested an additional ECC reported by Crockett *et al.*[92] and specific for 3d metal derivatives in dichloromethane, which gave *MW* = 520±228 g mol^{-1} (Figure S39).

EPR spectroscopy. A frozen 0.1 mM solution of **2** in CH_2Cl_2/toluene (1:1 v/v) gave the CW X-band EPR spectrum displayed in Figure 6b. The spectrum shows more than the three main resonances expected for a rhombic KD and can only be rationalized by considering that at least two species with much different SH parameters contribute to its structure. The simulation was then undertaken by considering the SH in Eq. (6) for two different spectral contributions (**2A** and **2B**) in variable proportion (Figure S40), using the same simulation protocol employed for the powder sample (see above). A fitting protocol has not been implemented due to the large number of parameters involved. The best simulations were obtained with the parameters gathered in Table 4 and a **2A**/**2B** molar ratio of 12:88. Due to the different environment and the sensibly decreased interaction between spins in the frozen glass, we reduced the anisotropic strain contributions to the linewidth and considered non-zero perpendicular components of the effective hyperfine tensor **A'** for both **2A** and **2B**. The minority contribution **2A** has SH parameters quite similar to those of solid **2**, suggesting it arises from a

hexacoordinated complex with two *trans* py ligands. Since ESI-MS and DOSY concurrently indicate that monomers prevail in solution, component **2A** can be assigned either to a residual fraction of intact dimers **2** or to *trans*-[Co(bdhb)(py)$_2$] monomers. However, the second spectral contribution (**2B**) has a quite different set of SH parameters, being characterized by pronounced easy-axis **g'** and **A'** anisotropies. Although strain and linewidth effects can severely bias quantitative determinations by EPR spectroscopy, it is apparent that a large fraction of cobalt(II) ions in **2** change their coordination environment upon dissolution. This might consist in either a different type of distortion from ideal octahedral symmetry while preserving hexacoordination (i.e. $B_2^0 < 0$ as opposed to $B_2^0 > 0$ in **2**)[97] or the loss of one or both py ligands, leading to penta- and tetracoordinated cobalt(II) centers, respectively. The latter hypothesis would be in reasonable agreement with the fast exchange of py ligands evidenced by ^{1}H NMR spectra and DOSY data. To support this interpretation, we undertook a detailed theoretical analysis of the structure, thermodynamic stability, and EPR parameters of [Co(bdhb)(py)$_x$] complexes (x = 0, 1, 2).

Conformational analysis and DFT structure optimization. To gain insight into the structure of the complexes in dichloromethane solution, we carried out a conformational search on the species [Co(bdhb)], [Co(bdhb)(py)], *cis*-[Co(bdhb)(py)$_2$], and *trans*-[Co(bdhb)(py)$_2$] by meta-dynamics simulations combined with semiempirical tight-binding methods.[98] After sorting and simplification, structures were optimized at the B97-3c DFT level,[99,100] including implicit solvation, and finally re-sorted to give 3, 19, 11, and 3 unique, energetically low-lying conformers for the above listed complexes, respectively. The structure of the thermodynamically most stable conformer of each compound is given in Figure 9a-d. Structural differences lie primarily in the torsion angles around the three C-C bonds involving the dimethylene bridges, in the coordination geometry, and in the rotation of the py ligands (when present) about the Co-py bond. For instance, the two most stable conformers of *trans*-[Co(bdhb)(py)$_2$] mainly differ in the dihedral angle between the two py rings, which are orthogonal in the ground conformer but coplanar in the first-excited conformer. The standard molar Gibbs free energy values (G°) at 298.15 K were then calculated at the same level of theory for each conformer and for the free py molecule, and used to evaluate cumulative G° data for either sides of the ligand dissociation equilibria:

cis/*trans*-[Co(bdhb)(py)$_2$] ⇌ [Co(bdhb)(py)] + py (9)

[Co(bdhb)(py)] + py ⇌ [Co(bdhb)] + 2py (10)

The results are displayed in Figure 9e and show that dissociation of the py ligands is a weakly endoergonic process. Considering for simplicity the thermodynamically most stable conformer of each complex, the removal of one and two py ligands from [Co(bdhb)(py)$_2$] results in ΔG° values of

0.9-1.4 kcal mol^{-1} for each dissociation step, with *cis*- and *trans*-[Co(bdhb)(py)$_2$] displaying almost identical thermodynamic stability. Further optimization of the thermodynamically most stable conformer of each complex and of free py at a higher level of theory (TPSSh-D4/def2-TZVP[101]) gave somewhat larger, but still positive $\Delta G°$ values (2.8-3.6 kcal mol^{-1}). The overall picture is then fully consistent with the information provided by experiments in diluted dichloromethane solution, which indicate partial dissociation of the py ligands. In particular, under the simplifying assumption that Eq. (9) is the only relevant equilibrium, the 68:32 ratio between coordinated and free py measured by DOSY yields [Co(bdhb)(py)] as the dominant complex in solution. With the overall concentration of Co^{2+} ions used in the experiment (0.0305 mol L^{-1}), an equilibrium constant of 0.035 is calculated at 298.15 K, which corresponds to $\Delta G°$ = 2.0 kcal mol^{-1}. It is rewarding that the experimental and calculated $\Delta G°$ values have the same sign and order of magnitude.

CASSCF/NEVPT2 calculations were also performed on the lowest Gibbs free energy conformers of each compound to compare the *g*-factors in their ground KD with those derived from the frozen solution EPR spectrum (Figure 6b and Table 4). Using the same procedure as before, for each compound we considered all the conformers in a standard Gibbs free energy window of 1 kcal mol^{-1}. A total of 10 different geometries were calculated, namely one for [Co(bdhb)], three for [Co(bdhb)(py)], four for *cis*-[Co(bdhb)(py)$_2$], and two for *trans*-[Co(bdhb)(py)$_2$]. The principal *g*-factors (labelled as $g_1' < g_2' < g_3'$) for the most stable conformer of each compound are given in Figure 9a-d, while the data for the remaining conformers are available in Table S8. None of these conformers has *g*-factors that perfectly match those of components **2A** and **2B** in the frozen solution spectrum; this is an expected result, considering the possible restraints imposed by the frozen solution matrix on molecular geometry and the exceedingly large sensitivity of *g*-factors to molecular structure. The ground conformer of tetracoordinated [Co(bdhb)] has a very pronounced easy-axis anisotropy, with g_1' and g_2' as small as 0.2 and a g_3' value of 7.2. These *g*-factors find no correspondence in the measured EPR spectrum. Furthermore, tetrahedral species usually display significantly larger molar extinction coefficients in the visible region of their electronic absorption spectra.[32] The three most stable conformers of pentacoordinated [Co(bdhb)(py)] have principal *g*-factors in the range 1.6-1.9, 2.0-2.3, and 6.6-8.2, thus denoting a predominant easy-axis anisotropy. Hexacoordinated *cis*-[Co(bdhb)(py)$_2$] has a less pronounced easy-axis character in its four most stable conformers, which display principal *g*-factors of 2.2-2.7, 3.2-3.8, and 6.2-6.9. The larger spread of values in [Co(bdhb)(py)] compared with *cis*-[Co(bdhb)(py)$_2$] correlates with the more pronounced geometrical differences among its most stable conformers (Figure S41). Overall, the expected EPR response of the studied conformers of [Co(bdhb)(py)] and *cis*-[Co(bdhb)(py)$_2$] matches well the observed spectral features of component **2B** (Table 4). Finally, the two most stable conformers of *trans*-[Co(bdhb)(py)$_2$], which differ only in

the relative orientation of the two pyridine rings (orthogonal or coplanar), have *g*-factors in the range 1.9-2.0, 3.9-5.0 and 5.2-6.3. The average *g*-factors (1.99, 4.48, 5.74) match remarkably well those of spectral contribution **2A** in the frozen solution EPR spectrum, suggesting that **2A** may actually originate from *trans*-[Co(bdhb)(py)$_2$].

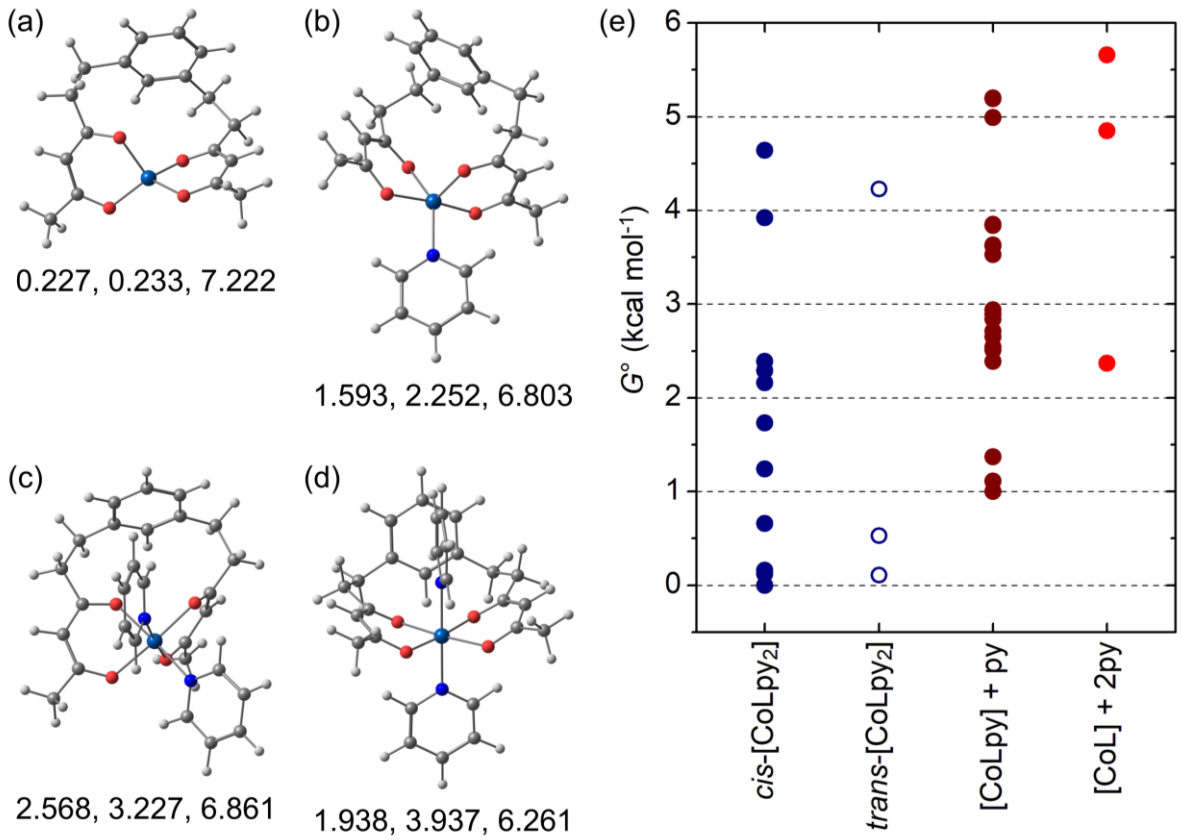

Figure 9. Structure of the thermodynamically most stable conformer of [Co(bdhb)] (a), [Co(bdhb)(py)] (b), *cis*-[Co(bdhb)(py)$_2$] (c), and *trans*-[Co(bdhb)(py)$_2$] (d), as resulting from DFT geometry optimization at the B97-3c level. Color code: C = grey, H = light grey, N = blue, O = red, Co = cobalt blue. The numbers under each structure are the principal values of the calculated **g'** tensor (g'_1, g'_2, g'_3). (e) Cumulative $G°$ data for either sides of Eqs. (9) and (10), evaluated by B97-3c DFT approach at 298.15 K. Each symbol is representative of a conformer. The bdhb^{2-} ligand is indicated with L to simplify notation. The value of $G°$ for the most stable conformer of *cis*-[Co(bdhb)(py)$_2$] is set to zero.

3. CONCLUSIONS

We carried out a comprehensive, multinuclear NMR study on the bis(β-diketone) H$_2$bdhb, first synthesized by Alberts and Cram,[5,10] in order to resolve its multiple keto-enolic equilibria in organic solution. Next, we explored the coordination chemistry of the bdhb^{2-} anion with cobalt(II) ions and isolated two 1:1 complexes (**1** and **2**). Compound **1**, analyzing as Co(bdhb)(H$_2$O)$_2$, was only isolated

in powder form and its solid-state structure is so far unknown. Compound $[Co_2(bdhb)_2(py)_4]$ (**2**) was obtained in crystalline form and has a dimeric structure in the solid state, with each $bdhb^{2-}$ ligand bound to two different high-spin cobalt(II) ions. Two axial pyridine molecules complete the tetragonally elongated octahedral geometry of the metals, which are more than 11 Å apart from each other. The cobalt(II) ions in **2** have a large easy-plane magnetic anisotropy ($D > 0$), with the ground KD about 140 cm^{-1} lower in energy than the first excited one. At temperatures below 7 K, compound **2** displays slow magnetic relaxation provided that a small static magnetic field is applied, with direct and Raman processes representing the dominant relaxation mechanisms. However, ESI-MS, UV-Vis, CW X-band EPR, and $^{1}H/^{2}H$ NMR data on pristine and isotopically labelled samples, including molecular weight determination by DOSY, showed that dissolution of **2** in an organic solvent like dichloromethane or THF causes profound structural alterations, with $[Co(bdhb)(py)_x]$ monomers representing the dominant species in solution. The observed dual structure in the crystalline state and in solution is likely a consequence of the conformationally flexible organic backbone of $bdhb^{2-}$, which can adopt different coordination modes. These mononuclear structures are clearly not accessible using more sterically constrained bis(β-diketonato) ligands, like those containing two acetoacetyl[102,103] or benzoylacetyl[33] residues directly connected to a central 1,3-arylene moiety.

Monomeric $[Co(bdhb)(py)_x]$ complexes ranging from tetra- ($x = 0$) to hexa-coordinated ($x = 2$) were then investigated theoretically to evaluate their structure, thermodynamic stability, and EPR response in the ground KD. The conformational landscape was first probed using meta-dynamics simulations and semiempirical tight-binding methods, and the energetically low-lying conformers so obtained were subsequently analyzed by DFT and CASSCF/NEVPT2 calculations. The stepwise removal of py ligands from *cis*- and *trans*-$[Co(bdhb)(py)_2]$ is predicted to be only weakly endoergonic (1-4 kcal mol^{-1} depending on the calculation protocol used), thus explaining the observed partial dissociation of py ligands. Furthermore, the calculated EPR parameters account fairly well for the different EPR spectra displayed by **2** in the crystalline state and in frozen solution. Among the probed $[Co(bdhb)(py)_x]$ structures, only the conformers of *trans*-$[Co(bdhb)(py)_2]$ have a similar easy-plane anisotropy to that of crystalline **2**, which features the same *trans*-CoO_4N_2 coordination geometry. By contrast, [Co(bdhb)], [Co(bdhb)(py)], and *cis*-$[Co(bdhb)(py)_2]$ have a predominant easy-axis character.

The reported results confirm that the coordination complexes of the $bdhb^{2-}$ ligand display a rich variability of structures in the solid state and in solution, thanks to the flexibility of ligand's backbone.

4. EXPERIMENTAL

General procedures. All chemicals were of reagent grade and used as received, unless otherwise noted. MeOH was dried using standard methods[104] and then stored over 3 Å molecular sieves. THF was pre-dried over KOH,[105] distilled from its sodium diphenylketyl solution, and stored over 4 Å molecular sieves before use. Dry CD_2Cl_2 used in NMR studies on **2** and **2-*d*$_{20}$** was deoxygenated through three freeze–pump–thaw cycles and stored over 4 Å molecular sieves. Pyridine was distilled over KOH (115–116 °C) and stored over KOH pellets prior to use. Hacac was dried over K_2CO_3[106,107] and distilled under reduced pressure (190 mmHg, 84–85 °C). Commercial NaH (60% mineral oil dispersion)[108] and *n*-BuLi solution (1.6 M in hexanes)[109] were titrated before use.

Combustion analysis was performed using a ThermoFisher Scientific Flash 2000 analyzer. FT-IR spectra were collected in ATR mode on a JASCO 4700 FT-IR spectrometer, between 400 and 4000 cm^{-1} and with a resolution of 2 cm^{-1}. Reflectance spectrum on finely ground crystals of **2** was collected with a standard diffuse reflectance attachment for a Jasco V-570 UV-Vis-NIR spectrometer. Electronic spectra were collected in THF, CH_2Cl_2, and CH_2Cl_2/toluene (1:1 v/v) using a Jasco V-570 UV-Vis-NIR spectrometer operating in double-beam mode (optical path length l = 0.1 or 1.0 cm). The following abbreviations are used in reporting FT-IR and UV-Vis-NIR data: s, strong; m, medium; w, weak; br, broad; sh, shoulder. ESI-MS measurements were conducted on a model 6310A Ion Trap LC-MS(n) instrument (Agilent Technologies) by direct infusion of THF solutions, in positive ion mode (the experimental spectra were shifted by m/z ~ 0.1-0.2 to account for a mismatch in the calibration of the instrument). The NMR spectra (^{1}H, ^{2}H, ^{13}C, ^{1}H–^{1}H COSY, ^{1}H–^{13}C E-HSQC, ^{1}H–^{13}C HMBC, and ^{1}H DOSY) were recorded at 298 K in acetone-d_6, DMSO-d_6, THF-d_8, CD_2Cl_2, or $CDCl_3$ on AVANCE III HD (600.13 and 150.90 MHz for ^{1}H and ^{13}C, respectively) and AVANCE400 (400.13 and 61.42 MHz for ^{1}H and ^{2}H, respectively) FT-NMR spectrometers from Bruker Biospin. CD_2Cl_2 solutions of complexes **2** and **2-*d*$_{20}$** were prepared at 0.03 M and 0.02 M concentration of Co^{2+} ions and measured using 5 mm airtight Young-valved NMR tubes from Norell. The spectra were analyzed and processed using TopSpin (version 4.3.0).[11] The chemical shifts (δ) are expressed in ppm downfield from tetramethylsilane (TMS) as external standard. The residual proton signals of acetone-d_6, DMSO-d_6, THF-d_8, CD_2Cl_2, and $CDCl_3$ were set at 2.05, 2.50, 1.72 [CH_2(3,4)], 5.32, and 7.26 ppm, respectively, while the $^{13}CD_3$ signal of acetone-d_6 was set at 29.84 ppm. The ^{2}H NMR spectrum of **2-*d*$_{20}$** was calibrated vs. the deuteron signal of CD_2Cl_2 at 5.32 ppm.[110] Alternatively, TMS was added as an internal standard. The exchange coupling constants (J) are expressed in Hz. The following abbreviations are used in reporting NMR data: s, singlet; br, broad; vbr, very broad; d, doublet; t, triplet; q, quartet; dd, doublet of doublets; pt, *pseudo*-triplet; m, multiplet. In the assignment of the ^{1}H NMR signals of H_2bdhb, the relative integrated intensities were found consistent with the number

of protons involved and the mole fraction of each tautomer. They are in general non-integer numbers and are omitted here for simplicity. ^{1}H DOSY measurements were carried out with a *ledbpgp2s* sequence (Bruker library) using bipolar gradient pulses,[111] tuning through the monodimensional sequence *ledbpgp2s1d* (Bruker library) the diffusion time (or *big delta*) and the gradient length (or *small delta*) to 0.015 s and 800 μs, respectively. The signal decay was fitted with a single exponential function using Bruker Dynamic Center software (version 2.8.3). The residual proton signal of the solvent was used as an internal reference for the normalization of measured *DC*s, following the procedure described by Stalke *et al*.[91]

Synthesis of 1,3-bis(3,5-dioxo-1-hexyl)benzene (H_2bdhb). In a three neck round bottom flask (250 mL) equipped with a magnetic stirrer, distilled Hacac (2.60 mL, 25.2 mmol) was dissolved in dry THF (50 mL) under nitrogen atmosphere obtaining a colorless solution. The system was cooled down to 0 °C, and NaH (50% oil dispersion, 1.2195 g, 25.41 mmol) was carefully added in small portions. This caused the evolution of hydrogen, and the reaction mixture became white and dense. After 30 min of stirring at 0 °C, *n*-BuLi in hexanes (1.53 M, 16.5 mL, 25.24 mmol) was added dropwise through a syringe to the reaction mixture, which gradually turned to pale-yellow. The resulting suspension was stirred at 0 °C for 30 min, and a colorless solution of α,α′-dibromo-*m*-xylene (2.2164 g, 8.3967 mmol) in 25 mL of dry THF (prepared under nitrogen atmosphere) was added dropwise with a syringe. The reaction mixture was stirred at 0 °C for 15 min and then overnight at 25 °C to give an orange suspension. Ice was carefully added to quench the unreacted NaH and *n*-BuLi, and the reaction mixture was poured into a stirred mixture of ice (100 g) and HCl 6 N (75 mL). The aqueous solution was extracted with Et_2O (4 × 70 mL), and the organic phases were combined, washed with H_2O (2 × 100 mL), and dried over Na_2SO_4. The desiccant was filtered off and the orange organic solution was evaporated to dryness, to give a red oil (3.3181 g) which was purified through gradient-elution flash chromatography (~ 75 g SiO_2 chromagel 60 Å, 35-70 μm, column Ø = 3.1 cm, column length = 24 cm; eluent CH_2Cl_2:acetone, flow rate = 20 mL/min; 100% CH_2Cl_2 for 30 min; from 100% CH_2Cl_2 to CH_2Cl_2:acetone 95:5 in 10 min; CH_2Cl_2:acetone 95:5 for 15 min), which gave H_2bdhb as a light red oil (1.8282 g, 6.0464 mmol, 72.0%). Replacing NaH (50% oil dispersion) with LiH (powder) or adding two molar equivalents of *n*-BuLi did not yield the desired product.

^{1}H NMR (acetone-d_6, 600.13 MHz, 298 K): δ = 15.65 (br, Hk_{KE}), 7.19 (t, $^3J(i,h)$ = 7.6, H$i_{\text{KE-KE}}$), 7.18 (t, $^3J(i,h)$ = 7.5, H$i_{\text{KE-KK}}$), 7.17 (t, $^3J(i,h)$ = 7.5, H$i_{\text{KK-KK}}$), 7.14 (s, H$j_{\text{KE-KE}}$), 7.11 (s, H$j_{\text{KE-KK}}$), 7.08 (s, H$j_{\text{KK-KK}}$), 7.07 (dd, $^3J(h,i)$ = 7.6, $^4J(h,j)$ = 1.5, Hh_{KE}), 7.05 (d, $^3J(h,i)$ = 7.5, Hh_{KK}), 5.65 (s, Hc_{KE}), 3.67 (s, Hc_{KK}), 2.88 (m, Hf_{KE}), 2.86 (m, He_{KK}), 2.84 (m, Hf_{KK}), 2.61 (pt, He_{KE}), 2.14 (s, Ha_{KK}), 2.01 (s, Ha_{KE}).

^{1}H NMR (DMSO-d_6, 400.13 MHz, 298 K): δ = 15.49 (br, Hk_{KE}), 7.18 (t, $^{3}J(i,h)$ = 7.5, H$i_{\text{KE-KE}}$), 7.17 (t, $^{3}J(i,h)$ = 7.5, H$i_{\text{KE-KK}}$), 7.16 (t, $^{3}J(i,h)$ = 7.4, H$i_{\text{KK-KK}}$), 7.09 (s, H$j_{\text{KE-KE}}$), 7.06 (s, H$j_{\text{KE-KK}}$), 7.05–6.94 (m, H$j_{\text{KK-KK}}$, Hh), 5.72 (s, Hc_{KE} in KE-KK), 5.71 (s, Hc_{KE} in KE-KE), 3.69 (s, Hc_{KK}), 2.85–2.69 (m, Hf_{KE}, Hf_{KK} and He_{KK}), 2.60 (m, He_{KE}), 2.11 (s, Ha_{KK}), 2.02 (s, Ha_{KE}).

^{1}H NMR (THF-d_8, 400.13 MHz, 298 K): δ = 15.62 (br, Hk_{KE}), 7.13 (t, $^{3}J(i,h)$ = 7.5, H$i_{\text{KE-KE}}$), 7.12 (t, $^{3}J(i,h)$ = 7.5, H$i_{\text{KE-KK}}$), 7.07 (s, H$j_{\text{KE-KE}}$), 7.05 (s, H$j_{\text{KE-KK}}$), 7.00 (d, $^{3}J(h,i)$ = 7.5, Hh_{KE}), 6.98 (m, Hh_{KK}), 5.54 (s, Hc_{KE}), 3.53 (s, Hc_{KK}), 2.85 (pt, Hf_{KE}), 2.82–2.73 (m, He_{KK} and Hf_{KK}), 2.55 (m, He_{KE}), 2.09 (s, Ha_{KK}), 1.97 (s, Ha_{KE}).

^{1}H NMR (CD_2Cl_2, 400.13 MHz, 298 K): δ = 15.49 (br, Hk_{KE}), 7.23–7.16 (m, Hi), 7.06–6.99 (m, Hh and Hj), 5.51 (s, Hc_{KE} in KE-KK), 5.50 (s, Hc_{KE} in KE-KE), 3.54 (s, Hc_{KK}), 2.88 (pt, Hf_{KE}), 2.86–2.77 (m, He_{KK} and Hf_{KK}), 2.57 (m, He_{KE}), 2.16 (s, Ha_{KK}), 2.02 (s, Ha_{KE}).

^{1}H NMR ($CDCl_3$, 400.13 MHz, 298 K): δ = 15.44 (br, Hk_{KE}), 7.21 (t, $^{3}J(i,h)$ = 7.3, H$i_{\text{KE-KE}}$), 7.20 (t, $^{3}J(i,h)$ = 7.4, H$i_{\text{KE-KK}}$), 7.06–6.98 (m, Hh and Hj), 5.48 (s, Hc_{KE} in KE-KK), 5.47 (s, Hc_{KE} in KE-KE), 3.55 (s, Hc_{KK}), 2.90 (pt, Hf_{KE}), 2.86–2.77 (m, He_{KK} and Hf_{KK}), 2.57 (pt, He_{KE}), 2.20 (s, Ha_{KK}), 2.04 (s, Ha_{KE}).

^{13}C NMR (acetone-d_6, 150.90 MHz, 298 K): δ = 204.43 (Cd_{KK}), 202.94 (Cb_{KK}), 194.96 (Cd_{KE}), 191.51 (Cb_{KE}), 142.22 (Cg_{KK} in KE-KK), 142.21 (C$g_{\text{KK-KK}}$), 141.98 (C$g_{\text{KE-KE}}$), 141.96 (Cg_{KE} in KE-KK), 129.31 (C$i_{\text{KE-KE}}$), 129.30 (C$i_{\text{KE-KK}}$), 129.28 (C$i_{\text{KK-KK}}$), 129.24 (C$j_{\text{KE-KE}}$), 129.21 (C$j_{\text{KE-KK}}$), 129.18 (C$j_{\text{KK-KK}}$), 126.94 (Ch_{KE}), 126.80 (Ch_{KK}), 100.59 (Cc_{KE}), 57.94 (Cc_{KK}), 45.43 (Ce_{KK}), 40.55 (Ce_{KE}), 31.93 (Cf_{KE}), 30.74 (Ca_{KK}), 29.98 (Cf_{KK}), 24.51 (Ca_{KE}).

ESI-MS (positive ion mode): m/z = 325.2 $[H_2bdhb + Na]^+$. IR (ATR): $\tilde{\nu}_{\text{max}}$ (cm^{-1}) = 3057 (w), 3024 (w), 3004 (w), 2957 (m), 2928 (w), 2865 (m), 2862 (m), 1724 (m), 1705 (m), 1600 (s), 1587 (s), 1487 (m), 1447 (m), 1415 (m), 1358 (m), 1300 (m), 1233 (m), 1207 (m), 1159 (m), 1131 (m), 1088 (m), 1026 (m), 1000 (m), 913 (m), 863 (m), 785 (s), 701 (s), 512 (m), 503 (m), 491 (w), 480 (w), 474 (w), 468 (m), 464 (m), 457 (m), 451 (m), 442 (m), 429 (w), 421 (m), 416 (m), 412 (m), 404 (m), 401 (m). UV–Vis–NIR (THF, b = 0.1 cm, $4.37 \cdot 10^{-4}$ M): λ_{max}/nm (ε/M^{-1} cm^{-1}) = 274 ($1.95 \cdot 10^4$). UV–Vis–NIR (CH_2Cl_2, b = 0.1 cm, $3.81 \cdot 10^{-4}$ M): λ_{max}/nm (ε/M^{-1} cm^{-1}) = 275 ($1.57 \cdot 10^4$).

Synthesis of "Co(bdhb)(H_2O)$_2$" (1). In a two neck round bottom flask (25 mL) equipped with a magnetic stirrer, anhydrous $Co(OAc)_2$ (419.9 mg, 2.372 mmol) was dissolved in dry MeOH (6.7 mL) under nitrogen atmosphere, obtaining a purple solution. In a vial, under nitrogen atmosphere, H_2bdhb (314.2 mg, 1.039 mmol) was dissolved in dry MeOH (3.4 mL) to yield an orange solution. This solution was then added dropwise with a syringe to the cobalt(II) acetate solution, causing the

immediate precipitation of a pink solid. The suspension was stirred at RT under inert atmosphere for 2 hours. The pink precipitate was collected by filtration through a fritted glass funnel (porosity G4) and washed with MeOH until colorless filtrate. The solid was then washed with Et_2O (~ 2 mL) and dried under vacuum to give a pale pink powder (346.5 mg, 0.8765 mmol, 84.3%). Elemental analysis (%) calcd. (found): C, 54.69 (54.44); H, 6.12 (6.12); N, 0.00 (0.00). ESI-MS (THF, positive ion mode): *m*/*z* = 359.2 ($[Co(bdhb)]^+$, 100.0%); 431.1 ($[Co(bdhb)(THF)]^+$, 27.9%); 502.8 ($[Co(bdhb)(THF)_2]^+$, 5.5%); 718.1 ($[Co_2(bdhb)_2]^+$, 2.4%); 719.0 ($[Co_2(bdhb)_2+H]^+$; 2.9%). ESI-MS (THF + py, positive ion mode): *m*/*z* = 359.2 ($[Co(bdhb)]^+$, 8.5%); 438.2 ($[Co(bdhb)(py)]^+$, 24.6%), 517.2 ($[Co(bdhb)(py)_2]^+$, 100.0%). IR (ATR): $\tilde{\nu}_{max}$ (cm^{-1}) = 3343 (m, br), 2957 (w), 2928 (w), 2861 (w), 1583 (s), 1559 (w), 1510 (s), 1489 (m), 1454 (m), 1436 (s), 1401 (s), 1361 (s), 1340 (m), 1285 (m), 1253 (m), 1191 (m), 1170 (w), 1158 (w), 1131 (m), 1085 (w), 1018 (m), 1007 (m), 941 (m), 922 (m), 899 (w), 891 (w), 788 (m), 773 (m), 702 (m), 607 (w), 565 (m), 546 (m), 491 (w), 464 (m), 460 (m), 447 (m), 435 (m), 432 (m), 425 (s), 418 (s), 414 (m), 405 (m), 401 (m). UV–Vis–NIR (THF, *b* = 0.1 cm): λ_{max}/nm (ε/M^{-1} cm^{-1}, *c*/molCo L^{-1}) = 291 ($1.95\cdot10^4$, $4.91\cdot10^{-4}$), 490 (37.7, $4.91\cdot10^{-3}$), 557 (sh, 19.3, $4.91\cdot10^{-3}$).

Synthesis of $[Co_2(bdhb)_2(py)_4]$ (2). Compound **1** (101.0 mg, 0.2555 mmol) was dissolved in dry THF (11 mL) to give a pink solution. Distilled pyridine (94 µL, 1.16 mmol) was added to the solution causing it to darken. The mixture was then stirred for 30 minutes and filtered. Upon slow diffusion of Et_2O vapors, orange-red blocks of **2** formed after approximately one week (55.1 mg, 0.0532 mmol, 41.7%). Elemental analysis (%) calc. (found): C, 64.99 (65.13); H, 5.84 (5.95), N, 5.41 (5.14). ESI-MS (positive ion mode): *m*/*z* = 359.1 ($[Co(bdhb)]^+$, 33.7%); 431.1 ($[Co(bdhb)(THF)]^+$, 4.0%); 438.2 ($[Co(bdhb)(py)]^+$, 100%); 517.1 ($[Co(bdhb)(py)_2]^+$, 48.4%). IR (ATR): $\tilde{\nu}_{max}$ (cm^{-1}) = 3070 (w), 3021 (w), 2956 (w), 2921 (w), 2859 (w), 1584 (s), 1558 (w), 1508 (s), 1486 (m), 1456 (s), 1446 (s), 1422 (s), 1354 (m), 1285 (m), 1246 (m), 1217 (m), 1190 (m), 1155 (w), 1124 (m), 1079 (m), 1072 (m), 1058 (w), 1037 (m), 1009 (m), 936 (m), 919 (m), 887 (w), 779 (m), 761 (m), 752 (s), 706 (m), 694 (s), 672 (m), 663 (m), 652 (m), 624 (m), 602 (w), 572 (w), 554 (m), 518 (m), 489 (w), 472 (w), 455 (m), 441 (m), 431 (m), 425 (m), 419 (s), 414 (m), 410 (m), 404 (m). UV-Vis-NIR reflectance spectra: λ_{max} (nm) = 475 (w, sh), 500 (w), 518 (w), 545 (w), 630 (w, sh), 1020 (s). UV–Vis–NIR (THF, *b* = 0.1 cm): λ_{max}/nm (ε/M^{-1} cm^{-1}, *c*/molCo L^{-1}) = 291 ($1.97\cdot10^4$, $3.79\cdot10^{-4}$), 488 (49.4, $3.79\cdot10^{-3}$), 555 (sh, 25.8, $3.79\cdot10^{-3}$). UV–Vis–NIR (CH_2Cl_2, *b* = 0.1 cm): λ_{max}/nm (ε/M^{-1} cm^{-1}, *c*/molCo L^{-1}) = 293 ($1.64\cdot10^4$, $3.75\cdot10^{-4}$), 500 (92.4, $3.75\cdot10^{-3}$), 590 (sh, 61.9, $3.75\cdot10^{-3}$). UV–Vis–NIR (CH_2Cl_2/toluene 1:1 v/v, *b* = 1 cm): λ_{max}/nm (ε/M^{-1} cm^{-1}, *c*/molCo L^{-1}) = 293 ($1.32\cdot10^4$, $1.88\cdot10^{-4}$), 495 (89, $3.76\cdot10^{-3}$), 590 (sh, 52, $3.76\cdot10^{-3}$). ^1H NMR (CD_2Cl_2, 400.13 MHz, 298 K): δ = ~147 (vbr), 53.9 (br,

4H, *o*-py), 43.4 (br), 36.0 (br), 27.4 (br), 25.4 (br), 14.4 (br, 4H, *m*-py), 11.5 (br), 2.9 (br), –2.1 (br, 2H, *p*-py), −12.8 (br).

Synthesis of [Co_2(bdhb)$_2$(py-d_5)$_4$] (2-d_{20}). Crystals of complex **2-*d*$_{20}$** were obtained following the same procedure described for **2**, replacing pyridine with pyridine-d_5. Single-crystal X-ray diffraction analysis on **2-*d*$_{20}$** gave the same unit cell parameters as for **2**. ^{1}H NMR (CD_2Cl_2, 400.13 MHz, 298 K): δ = 41.9 (br), 35.4 (br), 26.2 (br), 14.2 (br), 11.3 (br), 2.9 (br), −12.9 (br). ^{2}H NMR (CD_2Cl_2, 61.42 MHz, 298 K): δ = 53 (br, *o*-py), 15.3 (br, *m*-py), –0.6 (br, *p*-py).

X-ray Crystallography. An orange-red block-like crystal of **2**, prepared by liquid diffusion of *n*-hexane into a solution of **1** in THF/py (90:10 v/v) (Figure S11a), was cut from a twinned individual (Figure S11b), glued on a glass fiber with epoxy resin, and mounted on a Bruker-Nonius X8APEX diffractometer equipped with a Mo-Kα generator and area detector for data collection at RT. APEX2 v1.0-22 software[112] was used for the acquisition of matrix frames and data collection. Data reduction performed with SAINT v7.06A program[112] was followed by multi-scan absorption correction applied with SADABS v2.10.[112] Structure solution and full matrix least-squares refinement on F_o^2 were based on standard methods using SIR92,[113] SHELXL-2018/3,[114] and WINGX v2020.2[115] suite. All nonhydrogen atoms were refined anisotropically. Hydrogen atoms were treated as riding contributors in geometrically idealized positions with isotropic $U = 1.5U_{eq}$(C) or $1.2U_{eq}$(C) for CH_3 and other hydrogens, respectively. Methyl groups were found disordered over two positions rotated from each other by 60 degrees and were refined using AFIX 123 card with occupancy factors constrained to add up to one.

Magnetic measurements. Magnetic measurements in both DC and AC mode were conducted on a polycrystalline sample of **2**. The sample (10.21 mg) was grinded, pressed into a pellet and wrapped in Teflon® (9.2 mg). Magnetization (M) vs. T data were recorded at H = 1 kOe (between 2.0 and 36.0 K) or 10 kOe (between 38.0 and 300.0 K) on a Quantum Design MPMS instrument and used to calculate the susceptibility as $\chi = M/H$. Isothermal M vs. H data up to 50 kOe were collected at 2.0, 5.0, and 10.0 K. AC data were taken on a Quantum Design PPMS instrument at frequencies (ν) between 10 Hz and 10 kHz using a 6 Oe oscillating field. The depencency of χ_M'' on static magnetic field (H_{DC}) was preliminarily explored at T = 2.0 K for H_{DC} = 0 – 20 kOe. Subsequently, χ_M' vs. ν and χ_M'' vs. ν curves were measured at H_{DC} = 3 kOe in the range T = 2.0 – 6.5 K. Raw magnetic data were corrected for the sample-holder contribution and reduced using the appropriate molar mass (MW = 1034.3 g mol^{-1}) and estimated intrinsic diamagnetism ($\chi_M^{dia} = -517\cdot10^{-6}$ emu mol^{-1}). PHI v3.1.6 software[36] was used to fit the magnetic data to Eq. (1) or (2) with “Field Powder 12” command for powder integration.

Magnetic susceptibility measurements in solution were carried out at 298 K by Evans method[116,117] dissolving 7.1 mg of **2** in 0.45 mL of CD_2Cl_2 and using the residual proton signal of CD_2Cl_2 as a reference. The observed shift of protio impurities in the solvent, $\Delta f/f = 1.085 \cdot 10^{-6}$, was introduced in Grant's formula:[118,119]

$$\chi_{\mathrm{M}} \cong \frac{3\Delta f M}{4\pi f c} - \chi_{\mathrm{M}}^{\mathrm{dia}}$$

where c is the concentration of the solute in g mL^{-1}, to yield $\chi_{\mathrm{M}}T$ = 5.2 emu K mol^{-1} at 298 K.

CW-EPR Spectroscopy. All the CW-EPR spectra were recorded on a Bruker Elexys E500 spectrometer equipped with an SHQ cavity ($\nu \approx 9.40$ GHz). Low-temperature measurements were performed using an Oxford Instruments ESR900 continuous flow helium cryostat with temperature controlled by an Oxford Instruments ITC503. EPR spectra on solid samples were recorded on ≈ 3 mg of microcrystalline powders.

Computational Details. CASSCF[120] calculations were performed with ORCA 5.0.3,[121,122] including dynamic correlation with the NEVPT2 approach.[123] The experimental geometry of **2**, as obtained from the X-ray crystal structure, was employed for the calculation after replacing one of the Co atoms by Zn. The def2-TZVPP basis set was employed,[124,125] including the auxiliary basis sets for correlation and Coulomb fitting, for all the atoms. Relativistic effects were taken into account using the DKH (Douglas-Kroll-Hess) procedure.[126,127] The employed active space includes seven electrons in the five 3d orbitals of the cobalt(II) ion, CASSCF (7,5). All the states for the quartet state (10) and all the states for the doublet state (40) of the cobalt(II) ion were included. Single Aniso[128] as implemented in ORCA[129] was employed to calculate the matrix elements of the transition magnetic moments to have an estimation of the probability of transition between two different states of the molecules.

The conformer-rotamer ensemble sampling program CREST[98] was used for meta-dynamics conformational searches with the semiempirical tight-binding based quantum chemistry method GFN2-xTB.[130] Structures were assigned a neutral charge and a quartet spin state (S = 3/2), consistent with the high-spin state found in magnetic susceptibility measurements by Evans method. Implicit solvation by CH_2Cl_2 was described by the generalized Born and solvent accessible surface area model (GBSA). To cover as much conformational space as possible, multiple starting geometries were tested and, for each starting geometry, multiple CREST runs were carried out.[131] Ensemble sorting with removal of duplicates and rotamers was based on the following parameters: single-point energy window = 6 kcal mol^{-1}, RMSD threshold = 0.125 Å, single-point energy threshold between conformer pairs = 0.05 kcal mol^{-1}, lower bound for the rotational constant threshold = 0.01. The resulting

ensemble of unique conformers was simplified using Principal Component Analysis (PCA) and *k*-means clustering[99,132] to give representative low-energy structures. Their geometries were optimized by DFT using the composite approach B97-3c,[133] again assuming a neutral charge and a quartet spin state (S = 3/2), and describing implicit solvation by CH_2Cl_2 with the Conductor-like Polarizable Continuum Model (CPCM).[134] After structural optimization, vibrational frequencies were calculated in the harmonic approximation. No negative frequencies were found, indicating that (local) energy minima were reached in all cases. Thermochemical data were then computed at 1 atm and 298.15 K, assuming ideal gas behavior. All optimized structures had $\langle \hat{S}^2 \rangle$ in the range 3.77-3.81, hence close to the $S(S+1)$ value for S = 3/2 (3.75). Final ensemble sorting with the same parameters listed above gave 3, 19, 11, and 3 conformers for [Co(bdhb)], [Co(bdhb)(py)], *cis*-[Co(bdhb)$(py)_2$], and *trans*-[Co(bdhb)$(py)_2$], respectively. The thermodynamically most stable conformers of each compound were further optimized using the hybrid TPSSh[135–137] functional with the def2-TZVP basis set[125] and the D4 model for dispersion correction,[138] starting from the best geometries resulting from the B97-3c approach ($\langle \hat{S}^2 \rangle$ = 3.76). Calculations were carried out using the same protocols on the py molecule. Prior to use in the calculation of solution $\Delta G°$ values, the $G°$ values so-obtained were corrected by adding 1.894 kcal mol^{-1} to match the solution standard state (1 mol L^{-1}).[139] All calculations were made with ORCA 5.0.4,[121,140] using DEFGRID3, TightSCF, and TightOPT settings.

The magnetic properties of the thermodynamically most stable conformers of each compound were calculated using the same procedure described previously for **2**.

AUTHOR CONTRIBUTIONS

The manuscript was written through contributions of all authors. All authors have given approval to the final version of the manuscript.

CONFLICTS OF INTEREST

There are no conflicts of interest to declare.

DATA AVAILABILITY

The data supporting this article have been included as part of the ESI.† CCDC 2379443 contains the supplementary crystallographic data for compound **2**. These data can be obtained free of charge from The Cambridge Crystallographic Data Centre via www.ccdc.cam.ac.uk/structures (accessed on September 6, 2024), or by emailing data_request@ccdc.cam.ac.uk, or by contacting The Cambridge Crystallographic Data Centre, 12 Union Road, Cambridge CB2 1EZ, UK; fax: +44 1223 336033.

ACKNOWLEDGEMENTS

We thank dr. Maria Cecilia Rossi (Centro Interdipartimentale Grandi Strumenti, Università degli Studi di Modena e Reggio Emilia) and prof. Adele Mucci (Dipartimento di Scienze Chimiche e Geologiche e UdR INSTM, Università degli Studi di Modena e Reggio Emilia) for assistance in the realization of ^{1}H DOSY experiments and in the interpretation of the NMR spectra. Financial support from Ministerio de Ciencia, Innovación y Universidades (PID2021-122464NB-I00, TED2021-129593B-I00, and Maria de Maeztu CEX2021-001202-M grants) and from the Generalitat de Catalunya (2021-SGR-00286 grant) is acknowledged. E.R. also acknowledges the Generalitat de Catalunya for an ICREA Academia grant. We thank CSUC and BSC supercomputer centers for the computational resources. L.S and F.S. acknowledge the support of MUR through the grant Dipartimenti di Eccellenza 2023–2027 (DICUS 2.0, CUP B97G22000740001) to the Department of Chemistry ‘‘Ugo Schiff’’ of the University of Florence.

REFERENCES

1 N. N. Greenwood and A. Earnshaw, *Chemistry of the Elements*, Butterworth-Heinemann, Oxford, UK, 2nd edn., 1997.

2 V. Gold, Ed., *The IUPAC Compendium of Chemical Terminology*, International Union of Pure and Applied Chemistry (IUPAC), Research Triangle Park, NC, USA, 2nd edn., 2019.

3 B. Berti, M. Bortoluzzi, C. Cesari, C. Femoni, M. C. Iapalucci, R. Mazzoni, F. Vacca and S. Zacchini, *Inorg. Chem.*, 2019, **58**, 2911–2915.

4 C. Cesari, B. Berti, F. Calcagno, C. Femoni, M. Garavelli, M. C. Iapalucci, I. Rivalta and S. Zacchini, *Molecules*, 2021, **26**, 1529.

5 A. H. Alberts and D. J. Cram, *J. Am. Chem. Soc.*, 1979, **101**, 3545–3553.

6 T. Yamamura, K. Shirasaki, H. Sato, Y. Nakamura, H. Tomiyasu, I. Satoh and Y. Shiokawa, *J. Phys. Chem. C*, 2007, **111**, 18812–18820.

7 T. Yamamura, K. Shirasaki, Y. Shiokawa, Y. Nakamura and S.-Y. Kim, *J. Alloys Compd.*, 2004, **374**, 349–353.

8 K. Shirasaki, T. Yamamura and Y. Shiokawa, *J. Alloys Compd.*, 2006, **408**–**412**, 1296–1301.

9 M. Imperato, A. Nicolini, M. Boniburini, D. Sartini, E. Benassi, M. Chiesa, L. Gigli, Y.-K. Liao, A. Raza, E. Salvadori, L. Sorace and A. Cornia, *Inorg. Chem.*, 2024, **63**, 7912–7925.

10 A. H. Alberts and D. J. Cram, *J. Am. Chem. Soc.*, 1977, **99**, 3880–3882.

11 *TopSpin 4.3.0*, Bruker AXS Inc., Madison, WI, USA, 2023.

12 P. E. Hansen, *Pharmaceuticals*, 2021, **14**, 1189.

13 J. L. Burdett and M. T. Rogers, *J. Am. Chem. Soc.*, 1964, **86**, 2105–2109.

14 Z. Yoshida, H. Ogoshi and T. Tokumitsu, *Tetrahedron*, 1970, **26**, 5691–5697.

15 L. L. Lohr, J. C. Miller and R. R. Sharp, *J. Chem. Phys.*, 1999, **111**, 10148–10158.

16 S. E. Stavretis, E. Mamontov, D. H. Moseley, Y. Cheng, L. L. Daemen, A. J. Ramirez-Cuesta and Z.-L. Xue, *Phys. Chem. Chem. Phys.*, 2018, **20**, 21119–21126.

17 S. Gómez-Coca, A. Urtizberea, E. Cremades, P. J. Alonso, A. Camón, E. Ruiz and F. Luis, *Nat. Commun.*, 2014, **5**, 4300.

18 U. Baisch and R. Poli, *Polyhedron*, 2008, **27**, 2175–2185.

19 V. D. Vreshch, J.-H. Yang, H. Zhang, A. S. Filatov and E. V. Dikarev, *Inorg. Chem.*, 2010, **49**, 8430–8434.

20 R. N. Mukherjee, M. S. Venkateshan, M. D. Zingde and M. M. Dhingra, *J. Inorg. Nucl. Chem.*, 1976, **38**, 689–693.

21 R. C. Elder, *Inorg. Chem.*, 1968, **7**, 1117–1123.

22 A. Bencini, C. Benelli, D. Gatteschi and C. Zanchini, *Inorg. Chim. Acta*, 1980, **40**, X115–X116.

23 D. Gatteschi, *Inorg. Chim. Acta*, 1980, **40**, X21.

24 D. R. Eaton and K. L. Chua, *Can. J. Chem.*, 1973, **51**, 2632–2636.

25 D. A. Thornton, *Coord. Chem. Rev.*, 1990, **104**, 251–295.

26 J. T. Hashagen and J. P. Fackler, *J. Am. Chem. Soc.*, 1965, **87**, 2821–2824.

27 P. O. Dunstan, *Thermochim. Acta*, 1997, **303**, 209–218.

28 J. A. Happe and R. L. Ward, *J. Chem. Phys.*, 1963, **39**, 1211–1218.

29 G. N. La Mar, *J. Magn. Reson.*, 1969, **1**, 185–195.

30 W. Wang and H. Wei, *J. Chin. Chem. Soc.*, 1978, **25**, 185–194.

31 W. Liu and H. H. Thorp, *Inorg. Chem.*, 1993, **32**, 4102–4105.

32 A. B. P. Lever, *Inorganic electronic spectroscopy*, Elsevier, Amsterdam, New York, 2nd edn., 1984.

33 G. Aromí, H. Stoeckli-Evans, S. J. Teat, J. Cano and J. Ribas, *J. Mater. Chem.*, 2006, **16**, 2635–2644.

34 A. Bencini, C. Benelli, D. Gatteschi and C. Zanchini, *Inorg. Chem.*, 1980, **19**, 3027–3030.

35 F. Lloret, M. Julve, J. Cano, R. Ruiz-García and E. Pardo, *Inorg. Chim. Acta*, 2008, **361**, 3432–3445.

36 N. F. Chilton, R. P. Anderson, L. D. Turner, A. Soncini and K. S. Murray, *J. Comput. Chem.*, 2013, **34**, 1164–1175.

37 D. Gatteschi, R. Sessoli and J. Villain, *Molecular Nanomagnets*, Oxford University Press, Oxford, UK, 2006.

38 Y.-F. Deng, Z. Wang, Z.-W. Ouyang, B. Yin, Z. Zheng and Y.-Z. Zheng, *Chem. Eur. J.*, 2016, **22**, 14821–14825.

39 J. M. Zadrozny, J. Liu, N. A. Piro, C. J. Chang, S. Hill and J. R. Long, *Chem. Commun.*,

2012, **48**, 3927–3929.

40 W. Huang, T. Liu, D. Wu, J. Cheng, Z. W. Ouyang and C. Duan, *Dalton Trans.*, 2013, **42**, 15326–15331.

41 S. Vaidya, A. Upadhyay, S. K. Singh, T. Gupta, S. Tewary, S. K. Langley, J. P. S. Walsh, K. S. Murray, G. Rajaraman and M. Shanmugam, *Chem. Commun.*, 2015, **51**, 3739–3742.

42 S. Vaidya, S. K. Singh, P. Shukla, K. Ansari, G. Rajaraman and M. Shanmugam, *Chem. – A Eur. J.*, 2017, **23**, 9546–9559.

43 S. Mandal, S. Mondal, C. Rajnák, J. Titiš, R. Boča and S. Mohanta, *Dalton Trans.*, 2017, **46**, 13135–13144.

44 T. J. Woods, M. F. Ballesteros-Rivas, S. Gómez-Coca, E. Ruiz and K. R. Dunbar, *J. Am. Chem. Soc.*, 2016, **138**, 16407–16416.

45 M. A. Hay, A. Sarkar, G. A. Craig, L. Bhaskaran, J. Nehrkorn, M. Ozerov, K. E. R. Marriott, C. Wilson, G. Rajaraman, S. Hill and M. Murrie, *Chem. Sci.*, 2019, **10**, 6354–6361.

46 J. Acharya, A. Sarkar, P. Kumar, V. Kumar, J. Flores Gonzalez, O. Cador, F. Pointillart, G. Rajaraman and V. Chandrasekhar, *Dalton Trans.*, 2020, **49**, 4785–4796.

47 X. Hou, X. Wang, X. Liu, J. Wang, L. Tang and P. Ju, *New J. Chem.*, 2018, **42**, 8583–8590.

48 A. K. Mondal, J. Jover, E. Ruiz and S. Konar, *Chem. Commun.*, 2017, **53**, 5338–5341.

49 J. Vallejo, I. Castro, R. Ruiz-García, J. Cano, M. Julve, F. Lloret, G. De Munno, W. Wernsdorfer and E. Pardo, *J. Am. Chem. Soc.*, 2012, **134**, 15704–15707.

50 J. Acharya, A. Swain, A. Chakraborty, V. Kumar, P. Kumar, J. F. Gonzalez, O. Cador, F. Pointillart, G. Rajaraman and V. Chandrasekhar, *Inorg. Chem.*, 2019, **58**, 10725–10735.

51 Y.-F. Deng, M. K. Singh, D. Gan, T. Xiao, Y. Wang, S. Liu, Z. Wang, Z. Ouyang, Y.-Z. Zhang and K. R. Dunbar, *Inorg. Chem.*, 2020, **59**, 7622–7630.

52 M. R. Saber, M. K. Singh and K. R. Dunbar, *Chem. Commun.*, 2020, **56**, 8492–8495.

53 E. Colacio, J. Ruiz, E. Ruiz, E. Cremades, J. Krzystek, S. Carretta, J. Cano, T. Guidi, W. Wernsdorfer and E. K. Brechin, *Angew. Chem. Int. Ed.*, 2013, **52**, 9130–9134.

54 D. Wu, X. Zhang, P. Huang, W. Huang, M. Ruan and Z. W. Ouyang, *Inorg. Chem.*, 2013, **52**, 10976–10982.

55 R. Herchel, L. Váhovská, I. Potočňák and Z. Trávníček, *Inorg. Chem.*, 2014, **53**, 5896–5898.

56 R. Díaz-Torres, M. Menelaou, O. Roubeau, A. Sorrenti, G. Brandariz-de-Pedro, E. C. Sañudo, S. J. Teat, J. Fraxedas, E. Ruiz and N. Aliaga-Alcalde, *Chem. Sci.*, 2016, **7**, 2793–2803.

57 A. V. Palii, D. V. Korchagin, E. A. Yureva, A. V. Akimov, E. Y. Misochko, G. V. Shilov, A. D. Talantsev, R. B. Morgunov, S. M. Aldoshin and B. S. Tsukerblat, *Inorg. Chem.*, 2016, **55**, 9696–9706.

58 M. A. Palacios, J. Nehrkorn, E. A. Suturina, E. Ruiz, S. Gómez-Coca, K. Holldack, A. Schnegg, J. Krzystek, J. M. Moreno and E. Colacio, *Chem. – A Eur. J.*, 2017, **23**, 11649–11661.

59 C. Rajnák, F. Varga, J. Titiš, J. Moncol and R. Boča, *Inorg. Chem.*, 2018, **57**, 4352–4358.

60 D. Sertphon, K. S. Murray, W. Phonsri, J. Jover, E. Ruiz, S. G. Telfer, A. Alkaş, P. Harding and D. J. Harding, *Dalton Trans.*, 2018, **47**, 859–867.

61 L. Chen, S.-Y. Chen, Y.-C. Sun, Y.-M. Guo, L. Yu, X.-T. Chen, Z. Wang, Z. W. Ouyang, Y. Song and Z.-L. Xue, *Dalton Trans.*, 2015, **44**, 11482–11490.

62 A. K. Mondal, A. Mondal, B. Dey and S. Konar, *Inorg. Chem.*, 2018, **57**, 9999–10008.

63 F. Habib, I. Korobkov and M. Murugesu, *Dalton Trans.*, 2015, **44**, 6368–6373.

64 A. L. Pellegrino, C. Mezzalira, F. Mazzer, L. Cadi Tazi, A. Caneschi, D. Gatteschi, I. L. Fragalà, A. Speghini, L. Sorace and G. Malandrino, *Inorg. Chim. Acta*, 2022, **535**, 120851.

65 L. J. Berliner, G. R. Eaton and S. S. Eaton, Eds., *Distance Measurements in Biological Systems by EPR - Biological Magnetic Resonance*, Springer US, Boston, MA, USA, 2002, vol. 19.

66 K. N. Shrivastava, *Phys. status solidi*, 1983, **117**, 437–458.

67 S. T. Liddle and J. van Slageren, *Chem. Soc. Rev.*, 2015, **44**, 6655–6669.

68 S. Roy, I. Oyarzabal, J. Vallejo, J. Cano, E. Colacio, A. Bauza, A. Frontera, A. M. Kirillov, M. G. B. Drew and S. Das, *Inorg. Chem.*, 2016, **55**, 8502–8513.

69 C. Villa-Pérez, A. Zabala-Lekuona, I. J. Vitorica-Yrezabal, J. M. Seco, J. Cepeda, G. A. Echeverría and D. B. Soria, *Dalton Trans.*, 2024, **53**, 3254–3266.

70 A. Lunghi and S. Sanvito, *J. Phys. Chem. Lett.*, 2020, **11**, 6273–6278.

71 S. Mondal and A. Lunghi, *J. Am. Chem. Soc.*, 2022, **144**, 22965–22975.

72 A. Lunghi, *Sci. Adv.*, 2022, **8**, eabn7880.

73 F. Santanni, A. Albino, M. Atzori, D. Ranieri, E. Salvadori, M. Chiesa, A. Lunghi, A. Bencini, L. Sorace, F. Totti and R. Sessoli, *Inorg. Chem.*, 2021, **60**, 140–151.

74 F. Santanni, M. Briganti, G. Serrano, E. Salvadori, A. Veneri, C. Batistoni, S. F. Russi, S. Menichetti, M. Mannini, M. Chiesa, L. Sorace and R. Sessoli, *JACS Au*, 2023, **3**, 1250–1262.

75 A. Albino, S. Benci, L. Tesi, M. Atzori, R. Torre, S. Sanvito, R. Sessoli and A. Lunghi, *Inorg. Chem.*, 2019, **58**, 10260–10268.

76 E. Garlatti, A. Albino, S. Chicco, V. H. A. Nguyen, F. Santanni, L. Paolasini, C. Mazzoli, R. Caciuffo, F. Totti, P. Santini, R. Sessoli, A. Lunghi and S. Carretta, *Nat. Commun.*, 2023, **14**, 1653.

77 J. H. Van Vleck, *Phys. Rev.*, 1940, **57**, 426–447.

78 A. C. De Vroomen, E. E. Lijphart, D. Y. H. Prins, J. Marks and N. J. Poulis, *Physica*, 1972, **61**, 241–249.

79 L. Tesi, A. Lunghi, M. Atzori, E. Lucaccini, L. Sorace, F. Totti and R. Sessoli, *Dalton Trans.*, 2016, **45**, 16635–16643.

80 M. Amoza, L. Maxwell, N. Aliaga-Alcalde, S. Gómez-Coca and E. Ruiz, *Chem. – A Eur. J.*, 2021, **27**, 16440–16447.

81 M. Atzori, L. Tesi, S. Benci, A. Lunghi, R. Righini, A. Taschin, R. Torre, L. Sorace and R. Sessoli, *J. Am. Chem. Soc.*, 2017, **139**, 4338–4341.

82 L. Tesi, E. Lucaccini, I. Cimatti, M. Perfetti, M. Mannini, M. Atzori, E. Morra, M. Chiesa, A.

Caneschi, L. Sorace and R. Sessoli, *Chem. Sci.*, 2016, **7**, 2074–2083.

83 S. Stoll and A. Schweiger, *J. Magn. Reson.*, 2006, **178**, 42–55.

84 J. R. Miecznikowski, S. E. Zygmont, J. P. Jasinski, M. Kaur, E. Almanza, R. M. Kharbouch, S. C. Bonitatibus, E. E. Mircovich, P. Le Magueres, E. Reinheimer and A. C. Weitz, *Transit. Met. Chem.*, 2022, **47**, 127–137.

85 J. R. Pilbrow, *J. Magn. Reson.*, 1978, **31**, 479–490.

86 S. Ito and Y. Yano, *Bull. Chem. Soc. Jpn.*, 1984, **57**, 2824–2828.

87 Z. Szakács and Z. Sánta, in *Anthropic Awareness. The Human Aspects of Scientific Thinking in NMR Spectroscopy and Mass Spectrometry*, ed. C. Szantay Jr., Elsevier, Amsterdam, The Netherlands, 1st edn., 2015, pp. 257–289.

88 G. Kaysan, T. Rudszuck, L. Trapp, R. Balbierer, M. Kind and G. Guthausen, in *Annual Reports on NMR Spectroscopy*, ed. G. A. Webb, Royal Society of Chemistry, London, UK, 2022, pp. 47–93.

89 R. Evans, *Prog. Nucl. Magn. Reson. Spectrosc.*, 2020, **117**, 33–69.

90 R. Neufeld and D. Stalke, *Chem. Sci.*, 2015, **6**, 3354–3364.

91 S. Bachmann, R. Neufeld, M. Dzemski and D. Stalke, *Chem. Eur. J.*, 2016, **22**, 8462–8465.

92 M. P. Crockett, H. Zhang, C. M. Thomas and J. A. Byers, *Chem. Commun.*, 2019, **55**, 14426–14429.

93 M. Imperato, A. Nicolini, M. Borsari, M. Briganti, M. Chiesa, Y.-K. Liao, A. Ranieri, A. Raza, E. Salvadori, L. Sorace and A. Cornia, *Inorg. Chem. Front.*, 2024, **11**, 186–195.

94 S. Denis-Quanquin, F. Riobé, M. Delsuc, O. Maury and N. Giraud, *Chem. – A Eur. J.*, 2016, **22**, 18123–18131.

95 A. Raza, A. Mucci, A. Nicolini and A. Cornia, *Chemistry (Easton).*, 2022, **4**, 520–534.

96 A.-K. Kreyenschmidt, S. Bachmann, T. Niklas and D. Stalke, *ChemistrySelect*, 2017, **2**, 6957–6960.

97 A. Abragam and M. H. L. Pryce, *Proc. Roy. Soc. London. Ser. A. Math. Phys. Sci.*, 1951, **206**, 173–191.

98 P. Pracht, F. Bohle and S. Grimme, *Phys. Chem. Chem. Phys.*, 2020, **22**, 7169–7192.

99 M. Bursch, A. Hansen, P. Pracht, J. T. Kohn and S. Grimme, *Phys. Chem. Chem. Phys.*, 2021, **23**, 287–299.

100 G. Li, D. Li, M. Alshalalfeh, J. Cheramy, H. Zhang and Y. Xu, *Molecules*, 2023, **28**, 2571.

101 H. Jin and K. M. Merz, *J. Chem. Theory Comput.*, 2024, **20**, 2551–2558.

102 J. K. Clegg, Y. Kim and L. F. Lindoy, *J. Incl. Phenom. Macrocycl. Chem.*, 2015, **82**, 247–257.

103 A. J. Brock, J. K. Clegg, F. Li and L. F. Lindoy, *Coord. Chem. Rev.*, 2018, **375**, 106–133.

104 W. L. F. Armarego, *Purification of laboratory chemicals*, Butterworth-Heinemann, Oxford, UK, 8th edn., 2017.

105 A. B. C. Simas, V. L. P. Pereira, C. B. Barreto Jr., D. L. de Sales and L. L. de Carvalho,

Quim. Nova, 2009, **32**, 2473–2475.

106 K. G. Hampton, T. M. Harris and C. R. Hauser, *Org. Synth. Collect. Vol.*, 1973, **5**, 848.

107 K. G. Hampton, T. M. Harris and C. R. Hauser, *Org. Synth. Collect. Vol.*, 1988, **6**, 928.

108 *Aldrich Technical Bulletin No. AL-123. Quantitative Analysis of Active Metals and Metal Hydrides via Gas Buret*, Aldrich Chemical Company, Inc., Milwaukee, WI, USA, 1996.

109 B. E. Love and E. G. Jones, *J. Org. Chem.*, 1999, **64**, 3755–3756.

110 G. R. Fulmer, A. J. M. Miller, N. H. Sherden, H. E. Gottlieb, A. Nudelman, B. M. Stoltz, J. E. Bercaw and K. I. Goldberg, *Organometallics*, 2010, **29**, 2176–2179.

111 D. H. Wu, A. D. Chen and C. S. Johnson, *J. Magn. Reson. Ser. A*, 1995, **115**, 260–264.

112 *APEX2, SADABS, SAINT*, Bruker-AXS, Inc., Madison, Wisconsin, USA, 2012.

113 A. Altomare, G. Cascarano, C. Giacovazzo, A. Guagliardi, M. C. Burla, G. Polidori and M. Camalli, *J. Appl. Crystallogr.*, 1994, **27**, 435–435.

114 G. M. Sheldrick, *Acta Crystallogr. Sect. C Struct. Chem.*, 2015, **71**, 3–8.

115 L. J. Farrugia, *J. Appl. Crystallogr.*, 2012, **45**, 849–854.

116 D. F. Evans, *J. Chem. Soc.*, 1959, 2003–2005.

117 D. F. Evans, G. V. Fazakerley and R. F. Phillips, *J. Chem. Soc. A Inorganic, Phys. Theor.*, 1971, 1931–1934.

118 D. H. Grant, *J. Chem. Educ.*, 1995, **72**, 39–40.

119 C. Piguet, *J. Chem. Educ.*, 1997, **74**, 815–816.

120 B. O. Roos, in *Advances in Chemical Physics*, ed. K. P. Lawley, John Wiley & Sons, Ltd., New York, USA, 1987, pp. 399–445.

121 F. Neese, *WIREs Comput. Mol. Sci.*, 2022, **12**, e1606.

122 F. Neese, F. Wennmohs, U. Becker and C. Riplinger, *J. Chem. Phys.*, 2020, **152**, 224108.

123 C. Angeli, R. Cimiraglia and J.-P. Malrieu, *J. Chem. Phys.*, 2002, **117**, 9138–9153.

124 F. Weigend, *Phys. Chem. Chem. Phys.*, 2006, **8**, 1057–1065.

125 F. Weigend and R. Ahlrichs, *Phys. Chem. Chem. Phys.*, 2005, **7**, 3297–3305.

126 M. Douglas and N. M. Kroll, *Ann. Phys. (N. Y).*, 1974, **82**, 89–155.

127 B. A. Hess, *Phys. Rev. A*, 1986, **33**, 3742–3748.

128 L. F. Chibotaru and L. Ungur, *J. Chem. Phys.*, 2012, **137**, 64112.

129 M. Atanasov, D. Aravena, E. Suturina, E. Bill, D. Maganas and F. Neese, *Coord. Chem. Rev.*, 2015, **289**–**290**, 177–214.

130 S. Grimme, *J. Chem. Theory Comput.*, 2019, **15**, 2847–2862.

131 H. Wang, M. Heger, M. H. Al-Jabiri and Y. Xu, *Molecules*, 2021, **27**, 38.

132 J. Shao, S. W. Tanner, N. Thompson and T. E. Cheatham, *J. Chem. Theory Comput.*, 2007, **3**, 2312–2334.

133 J. G. Brandenburg, C. Bannwarth, A. Hansen and S. Grimme, *J. Chem. Phys.*, 2018, **148**, 064104.

134 V. Barone and M. Cossi, *J. Phys. Chem. A*, 1998, **102**, 1995–2001.

135 J. Tao, J. P. Perdew, V. N. Staroverov and G. E. Scuseria, *Phys. Rev. Lett.*, 2003, **91**, 146401.

136 V. N. Staroverov, G. E. Scuseria, J. Tao and J. P. Perdew, *J. Chem. Phys.*, 2003, **119**, 12129–12137.

137 V. N. Staroverov, G. E. Scuseria, J. Tao and J. P. Perdew, *J. Chem. Phys.*, 2004, **121**, 11507–11507.

138 E. Caldeweyher, S. Ehlert, A. Hansen, H. Neugebauer, S. Spicher, C. Bannwarth and S. Grimme, *J. Chem. Phys.*, 2019, **150**, 154122.

139 C. J. Cramer, *Essentials of Computational Chemistry: Theories and Models*, John Wiley & Sons, Ltd, Chichester, UK, 2nd edn., 2004.

140 F. Neese, *WIREs Comput. Mol. Sci.*, 2012, **2**, 73–78.